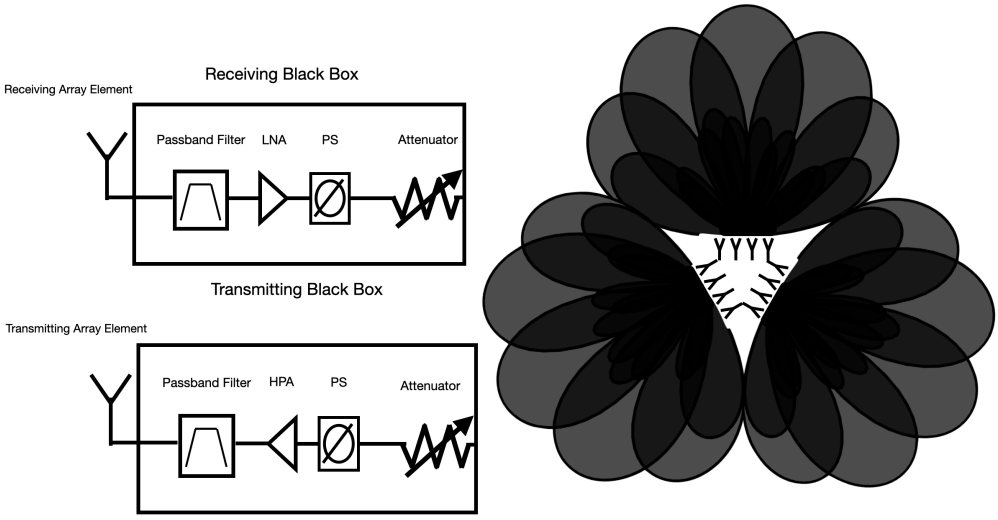


# Over the Air Phased Array Calibration at 100 GHz

Master's thesis in Information and Communication Technology

Dani Tahhan

DEPARTMENT OF ELECTRICAL ENGINEERING

Chalmers University of Technology
Gothenburg, Sweden 2024
www.chalmers.se

Master's thesis 2024

# Over the Air Phased Array Calibration at 100 GHz

Dani Tahhan


CHALMERS

DEPARTMENT OF ELECTRICAL ENGINEERING
Chalmers University of Technology
Gothenburg, Sweden 2024

Over the Air Phased Array Calibration at 100 GHz
Dani Tahhan



Supervisor: Azadeh Tabeshnezhad, Department of Electrical Engineering
Supervisor: Johan Wettergren, Qamcom Company
Examiner: Thomas Eriksson, Department of Electrical Engineering

Master's Thesis 2024
Department of Electrical Engineering
Chalmers University of Technology
SE-412 96 Gothenburg
Telephone +46 31 772 1000

Cover: The block diagram of the calibrated transceiver and the radiation pattern of three phased array antennas, each comprising four elements, for 360° coverage.

Typeset in LaTeX
Printed by Chalmers Reproservice
Gothenburg, Sweden 2024

Over the Air Phased Array Calibration at 100 GHz
Dani Tahhan
Department of Electrical Engineering
Chalmers University of Technology

# Abstract

This thesis presents a comprehensive analysis of building and calibrating a 100 GHz transceiver with a 10 GHz bandwidth, focusing on component selection based on performance characteristics and incorporating linear phased array antennas of various sizes. The study emphasizes the role of uncertainty sources such as impedance mismatches, temperature fluctuations, and structural errors in antenna performance, analyzing arrays of 4, 8, and 16 elements to understand size effects on antenna behavior and achieve a coverage range of $\pm 60°$.

Key findings indicate that 4-bit phase shifters can closely replicate theoretical beam patterns with minimal deviation, while amplitude perturbations significantly impact 8-element arrays more than 16-element arrays, with 4-element arrays displaying greater perturbation tolerance. Temperature-induced phase shifts necessitate calibration for the 4-element array at extreme temperatures, whereas 8-element arrays show reduced sensitivity.

The thesis further evaluates two calibration algorithms designed to address systematic phase errors caused by manufacturing error, such as bent slab distortion and irregular phase errors. The mREV algorithm required multiple iterations to align the radiation pattern with theoretical predictions, while the simpler ON/OFF method achieved similar results with a single iteration. Notably, the number of iterations needed for the mREV algorithm decreases as the number of array elements increases, enhancing calibration efficiency.

# Acknowledgment

Firstly, I would like to thank my supervisor, Johan Wettergren, for giving me the opportunity to undertake this amazing thesis at Qamcom. His warm welcome and guidance during my time at Qamcom constantly pushed me to challenge myself and learn from his expertise. I would also like to express my gratitude to my supervisor at Chalmers, Azadeh Tabeshnezhad, for her invaluable support in improving my report writing. Additionally, I thank my examiner, Thomas Eriksson, for being available to answer my questions. A big thanks goes to my wife, who supported me throughout this journey. Without her help, I would not have been able to achieve what I have during my studies. I have learned so much during my time at Chalmers and have gained many friends for whom I am deeply thankful.

Dani Tahhan, Gothenburg, May 2024

# List of Acronyms

**PS** Phase Shifters
**DPS** Digital Phase Shifters
**5G** Fifth-Generation Mobile Communication
**OTA** Over-The-Air
**AUT** Antenna Under Test
**mmW** Millimeter-Wave
**CATR** Compact Antenna Test Range
**ERP** Effective Radiated Power
**G/T** Gain-to-Noise Ratio
**DAC** Digital-to-Analog Converter
**MEMS** Micro-Electromechanical System
**RE-MEMS** Reflective Micro-Electromechanical System
**RF-MEMS** Radio Frequency Micro-ElectroMechanical Systems
**MMIC** Microwave Monolithic Integrated Circuit
**CMOS** Complementary Metal-Oxide Semiconductor
**BiCMOS** Bipolar Complementary Metal-Oxide Semiconductor
**DPD** Digital Pre-Distortion
**LSB** Least Significant Bit
**RMS** Root Mean Square
**LNA** Low Noise Amplifier
**PA** Power Amplifier
**SNR** Signal-to-Noise Ratio
**NF** Noise Figure
**HEMT** High-Electron-Mobility Transistor
**pHEMT** Pseudomorph High-Electron-Mobility Transistor
**mHEMT** Metamorphoic High-Electron-Mobility Transistor
**GaAs** Gallium-Arsenide
**InP** Indium-Phosphide
**TWT** Traveling Wave Tube
**SiGe** Silicon Germanium
**BPF** Band-Pass Filter
**iBPF** Interdigirtal Band-Pass Filter

# Contents

# List of Figures

# List of Tables

# 1

# Introduction

Recent years have seen a surge in data consumption driven by new features and applications, necessitating access to broader spectrum resources. This requirement has steered interest towards mmWave wireless communication, known for offering expansive bandwidths that align with these increasing demands [1]. The advent of 5G (fifth-generation mobile communication) marks a significant leap forward, enhancing capacity, coverage, and connectivity beyond what previous generations achieved [2]. The move to higher frequency bands is particularly appealing to the industry, given the underutilized spectrum resources and the superior quality of service these frequencies can deliver [3]. In this context, developing transceivers for the W-band (75 GHz-110 GHz) emerges as an optimal strategy for wireless transmission. The substantial bandwidth available in this range (up to 35 GHz) supports large-capacity data transmission, while the lower atmospheric attenuation at these frequencies, less than 0.5 dB/km, facilitates long-distance communication [1] [4].

As the frequency used for signal transmission increases, the wavelength of the signal decreases, leading to greater path loss. To counteract this attenuation, it is necessary to enhance the antenna gain. While increasing the antenna size can provide higher gain, this approach is often impractical due to implementation challenges and the increased complexity of the transceiver [5] [6]. A more efficient method to boost gain involves augmenting the number of radiating elements in what is known as an "Array Antenna," allowing them to work together constructively. This enhancement is facilitated by phase shifters (PSs), which introduce specific phase shifts to the elements within the array, resulting in what is termed a phased array antenna. The introduction of phase shifts among the array elements serves one main purpose as it enables the antenna to steer its beam directionally without physical movement and to generate multiple beams simultaneously. The complex weights of individual elements, the spacing between elements in the array, and the introduced phase shifts are crucial in determining the antenna's characteristics. This allows for flexibility in antenna design, accommodating various applications effectively [6] [7].

Meeting design objectives presents a significant challenge in antenna engineering, influenced by various factors that can negatively affect performance. Issues such as structural component inaccuracies, assembly errors, variations in radiation patterns of individual elements, and amplitude and phase discrepancies among RF elements contribute to amplitude and phase errors. These errors can lead to performance degradation, evident in altered radiation patterns and heightened sidelobe levels [8] [9]. Additionally, factors like temperature effects on performance and compo-

nent aging must also be accounted for, highlighting the necessity for effective and precise calibration in both antenna testing and manufacturing [9] [10]. Calibration methods are categorized based on the location of measurement components: internal calibration, where measurement components are embedded within the phased array, and external, or over-the-air (OTA) calibration, where measurements occur outside the antenna. Internal calibration involves adding calibration circuits to each RF branch, a method deemed inefficient due to its complexity. Conversely, OTA calibration avoids these challenges by calibrating based on the signals transmitted or received by the antenna under test (AUT), regardless of whether the AUT operates in the transmitting or receiving chain. This approach depends on the specific procedure for signal measurement, distinguishing the OTA calibration method and offering a more straightforward and efficient calibration process. OTA calibration methods are vulnerable to environmental disturbances and multipath effects, which can compromise calibration accuracy. Addressing these challenges requires extensive anechoic chambers, significantly increasing the cost. Moreover, the considerable space loss involved further impacts the dynamic range of the testing system negatively[8] [10] [11] [12].

# 2

# Aims and Objectives

Given the desirability of frequencies beyond 100 GHz, ensuring flawless operation of RF hardware becomes a critical challenge within this frequency range. Consequently, the primary aim is to implement calibration algorithms addressing amplitude and phase calibration for a phased array antenna. To achieve this, the calibration process needs to be executed over the air. Calibrating the signal across each pathway individually proves inefficient, as calibration is required at every step before signal transmission. The calibration process encompasses both transmitting and receiving modes, thus a thorough investigation into the corresponding hardware at higher frequencies and various temperatures is required. Specifically, in the transmitting mode, a meticulous examination of a crucial component, that is high power amplifier (HPA), is imperative. On the other hand, in the receiving mode, it is the Low-Noise Amplifier (LNA) that demands careful scrutiny. Furthermore, it is essential to account for the quantization errors introduced by the PSs, as compensating for these errors is a crucial aspect of the calibration process. This thesis seeks to address the following objectives:

1. Evaluate the accuracy of the chosen calibration algorithm in comparison to the benchmarking method at high-frequency bands. This investigation aims to determine the feasibility of implementing existing algorithms and identify necessary adjustments for calibrating the phase of phased arrays at the specified frequencies.
2. Investigate various digital components, such as PSs and attenuators, to identify the errors introduced by these components. Understand the relationship between these errors and high frequencies. Recognizing and characterizing these errors is essential for the calibration process, particularly at the frequencies under investigation.
3. Examine the impact of various sources of uncertainty, including temperature fluctuations, impedance mismatches, and mechanical errors during antenna manufacturing, on the performance of transmitting/receiving chains. Understanding how these uncertainties degrade performance is crucial to determining the necessary calibration.

# 3
# Theory & Background

In this section, the foundational aspects of measurement methods, phased array technology, and the electrical components utilized in constructing transmitting and receiving chains are explored, along with the underlying theory. Additionally, theoretical insights to understand the characteristics of these components are provided. Also, the sources of uncertainty are discussed and theoretical models that simulate the impact of these sources on performance are explained.

## 3.1 S-parameters

S-parameters play a significant role in the design and analysis of microwave devices, as well as in their simulation and performance evaluation. They are essential for characterizing both active devices, like transistors and diodes, and passive components, such as transmission lines, capacitors, resistors, and inductors. S-parameters vary with frequency, reflecting how RF devices handle signal reflection and transmission at diverse frequencies. As the frequency shifts, so do the S-parameter values, influencing device behavior throughout the RF spectrum. A common approach to describe a device or circuit is through the two-port network model, which treats the device as a black box with designated input and output ports [13] [14]. The relationship between the incident and outgoing waves at each port is encapsulated by the S-parameters matrix, as illustrated in [15] by the equation below:

$$\begin{bmatrix} b_1 \\ b_2 \end{bmatrix} = \begin{bmatrix} S_{11} & S_{12} \\ S_{21} & S_{22} \end{bmatrix} \begin{bmatrix} a_1 \\ a_2 \end{bmatrix} \tag{3.1}$$

where $a$ and $b$ denote the incident and reflected power waves, respectively. The diagonal elements of the S-parameters matrix correspond to the reflection coefficients at each port, indicating the proportion of the incident wave that is reflected back from a single port. These parameters, referred to as return loss, are ideally minimized to indicate that the energy reflected due to impedance mismatch is low. These coefficients can be expressed according to [15] as follows:

$$S_{11} = \left.\frac{b_1}{a_1}\right|_{a_2=0} = \Gamma_1 \tag{3.2}$$

$$S_{22} = \left.\frac{b_2}{a_2}\right|_{a_1=0} = \Gamma_2 \tag{3.3}$$

where $\Gamma$ is the reflection coefficient. Conversely, the off-diagonal elements of the matrix indicate the amount of signal transmitted through the device at a given fre-

quency, that is, from one port to another. These elements are known as transmission coefficients and are represented as in [15] as follows:

$$S_{12} = \left.\frac{b_1}{a_2}\right|_{a_1=0} = T_1 \tag{3.4}$$

$$S_{21} = \left.\frac{b_2}{a_1}\right|_{a_2=0} = T_2 \tag{3.5}$$

where $T$ is the transmission coefficient. S-parameters are applicable to multi-port devices as well, with the S-matrix for an N-port device being expressible in the following manner:

$$\begin{bmatrix} b_1 \\ b_2 \\ \vdots \\ b_N \end{bmatrix} = \begin{bmatrix} S_{11} & S_{12} & \cdots & S_{1N} \\ S_{21} & \ddots & & \vdots \\ \vdots & & \ddots & \vdots \\ S_{N1} & \cdots & \cdots & S_{NN} \end{bmatrix} \begin{bmatrix} a_1 \\ a_2 \\ \vdots \\ a_N \end{bmatrix} \tag{3.6}$$

## 3.2 Antenna Measurement Methods

One of the primary and critical steps is measuring antenna parameters to ensure adherence to specified characteristics. While possessing extensive knowledge in antenna engineering and theory is essential, accurate measurements require advanced and costly equipment. Various measurement methods, evolving since the 1960s, can be broadly categorized into far-field and near-field setups [16].

Primarily, in the far-field, antenna parameters are directly measured by exposing the AUT to a plane wave. One type of far-field setup is the ground reflection range, where a uniform amplitude and phase distribution is achieved along with specular reflections from the ground. Another type is the free space range, where the AUT is illuminated within an anechoic chamber to minimize environmental reflections. Using an anechoic chamber proves to be the most suitable setup for millimeter-wave (mmW) antenna measurements. This is attributed to the fact that this type of antennas decrease in size as the frequency increases. To establish a plane wave, the distance between the AUT and illuminating antenna should be $\geq \ 2D^2/\lambda$, where $D$ denotes the maximum dimension of the AUT, and $\lambda$ denotes the wavelength. This implies that no large chambers are required since the far-field distance does not surpass 1 $m$ [16]. Since this study concentrates on the 100 GHz frequency, $\lambda$ is 0.003 $m$. Therefore, any antenna with $D$ smaller than 0.035 $m$ meets the far-field criterion within a 1-meter chamber.

Anechoic chambers boast features such as the ability to control the test environment, all-weather capability, and the minimization of electromagnetic interference for antenna measurements. These characteristics make this setup the most widely adopted for the purpose of antenna measurements. The key components required for antenna measurements, including a transmitter, receiver, signal source, positioning system, data processing system, and vector network analyzer [16]. The

performance of the AUT depends on the electrical components in its chain, indicating that whether the AUT serves as a transmitter or receiver is contingent on the performance of these components. For the remainder of the thesis, it is anticipated that a probe antenna serves as the illuminating antenna; henceforth, both antennas are referred to as AUT and probe antenna. The chamber's walls are covered with in RF absorber, with its thickness inversely proportional to the operating frequency. In simpler terms, higher frequencies necessitate thinner RF-absorbing material to maintain a specified level of reflectivity performance. The setup of this method is illustrated in Figure 3.1.

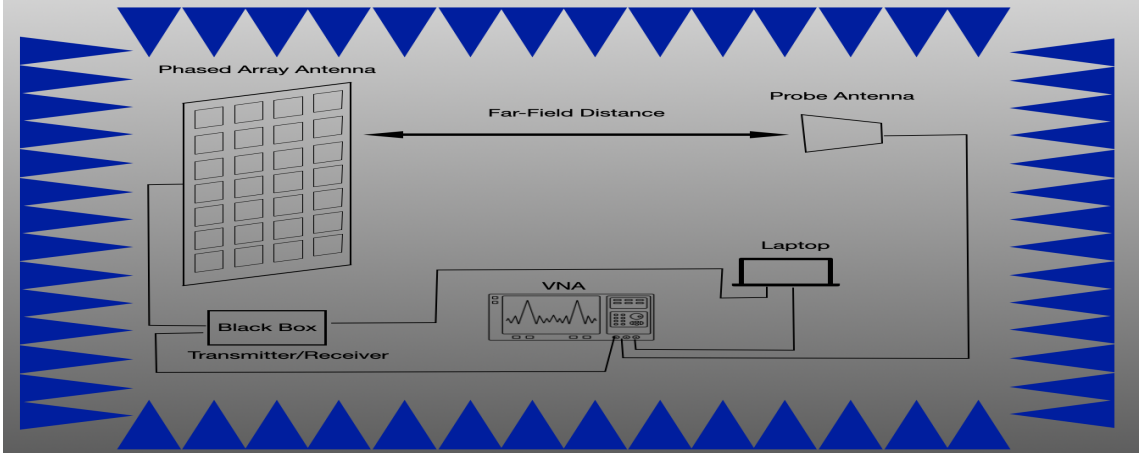


Figure 3.1: Architecture of the far-field measurement setup in anechoic chamber [16]

Another approach to conducting far-field antenna measurements for large antennas involves the use of a Compact Antenna Test Range (CATRs). This configuration closely resembles the anechoic chamber method with a notable difference that is the challenge of obtaining a sufficient far-field distance. To overcome this challenge, a parabolic reflector is employed, converting the spherical waves from the transmitting antenna into plane waves directed towards the AUT. A significant drawback of this setup is its demand for highly accurate surfaces at mmW frequencies. For instance, at 75 GHz, the RMS error of the surface must be as low as 40 $\mu m$. Antenna radiation characteristics can be derived by measuring the near-field distribution of the AUT as well. Essentially, far-field radiation characteristics can be extrapolated by applying transformation methods to the near-field measurements. A crucial condition for this method is that the separation between two samples in the near-field measurement must be smaller than $\lambda/2$ to meet the Nyquist criterion. This implies the necessity for very dense sampling in mmW antenna measurements.

## 3.3 Phased Array Antenna

The radiation pattern of a single-element antenna typically exhibits a broad coverage, resulting in relatively low directivity. For long-distance communication, directive antennas, which can focus energy more efficiently in a specific direction and

thus achieve higher gains, are essential. Rather than increasing the physical size of the antenna to enhance directivity and gain, a highly directive antenna can be achieved by organizing multiple antenna elements into an array. This assembly, usually consisting of identical elements, creates both an electrical and geometrical configuration that optimizes directivity. Through this method, the total electric field is a composite of the fields from each element, orchestrated to reinforce each other constructively in preferred directions while cancelling out in others through destructive interference. The resultant radiation pattern of the array is influenced by several key factors, including the spatial arrangement of the elements, the amplitude and phase excitation of each element, the spacing between elements, and the inherent radiation pattern of the individual elements [17] [18].

Phased array antennas, also known as electronically scanned arrays, have found widespread applications in automotive and wireless communication systems. Their compact size and the ability to steer the beam without mechanical rotators make them versatile and less expensive. These antennas are appealing not just because of beam steering capabilities, they also offer the ability to create multiple beams aimed at specific directions, thanks to the assistance of PSs. Originally introduced in the early 1960s for radar applications, particularly to track fast-moving targets, this technology was initially considered expensive and complex. Over time, advancements have enhanced its utility in various domains [19] [20].

In a M×N-element planar array antenna, the aggregate electric field as a function of the elevation angle $\phi$ and the azimuth angle $\theta$ is delineated as per [17] [7] by the equation:

$$E(\theta,\phi)_{total} = \sum_{m=1}^{M}\sum_{n=1}^{N} E_{m,n} I_{m,n} e^{j(m-1)(n-1)(kd(\sin\theta\cos\phi+\sin\theta\sin\phi)+\psi_{m,n})} \tag{3.7}$$

$$\psi_{m,n} = -kd(m-1)(n-1)(\sin\theta_0\cos\phi_0 + \sin\theta_0\sin\phi_0) \tag{3.8}$$

Here, $k$ represents the wave number, equivalent to $2\pi/\lambda$, $\lambda$ is the wavelength; $d$ denotes the spacing between elements; $\psi_{m,n}$ specifies the phase shift at the $[m,n]$-th element; and $I_{m,n}$ and $E_{m,n}$ correspond to the amplitude excitation and the electric field of the individual $[m,n]$-th element in the array, respectively. In case progressive linear phase shift is used to steer the beam at the intended direction $(\phi_0,\theta_0)$, $\psi_{m,n}$ is obtained as in 3.8.

Understanding the beamwidth of an antenna is crucial, as it indicates how widely the antenna's main beam spreads across different angles. Specifically, the beamwidth is defined by the angular width of the main lobe where the power falls to half of its peak value, a characteristic known as the half-power beamwidth or $\theta_{3dB}$. This is because at these points, the power reduction is 3 dB, corresponding to half the peak power. In phased arrays, the half-power beamwidth, $\theta_{3dB}$, varies with the steering angle, $\theta_0$, and can be described by the following relationship according to [20]:

$$\theta_{3dB} = \frac{0.886\lambda}{Md\cos\theta_0}. \tag{3.9}$$

Another essential attribute of an antenna is its directivity, denoted as $D$, representing the peak value of the directive gain, $D(\theta)$. Directive gain itself is the measure of radiation intensity in a specific direction, $U(\theta)$, relative to the average radiation power dispersed across all directions. Higher directivity is advantageous as it signifies that a greater portion of the radiated power is focused in a specific direction. The formulas for these parameters are detailed as follows in [20]:

$$D(\theta, \phi) = \frac{4\pi U(\theta, \phi)}{\int_{\phi=0}^{2\pi} \int_{\theta=0}^{\pi} U(\theta, \phi) \sin\theta d\theta d\phi} \tag{3.10}$$

$$D = max(D(\theta, \phi)). \tag{3.11}$$

The successful communication distance between a transmitter and receiver hinges on several factors. For a one-way communication link, the range $R$ can be expressed according to [19] by the equation:

$$P_t = \frac{P_r G A_e}{4\pi R^2} \tag{3.12}$$

where $P_t$ represents the power transmitted, $P_r$ is the power received, $G$ denotes the antenna gain, and $A_e$ is the effective area of the receiving antenna.

### 3.3.1 Slot Array Antenna at 100 GHz

A one-dimensional slot array antenna utilizing ridge gap waveguide technology is described in [21]. Operating at 100 GHz, this antenna offers an extensive scanning capability of ±60 degrees, maintaining a stable active reflection coefficient throughout this range, attributed to the use of a compact "half-wall" decoupling structure. Essentially, this structure is a metallic barrier that covers half of the slots. Measurements indicate that the $S_{11}$ parameter remains under -3 dB across a bandwidth spanning from 96 GHz to 106 GHz for all scanning angles. The antenna achieves an overall efficiency of 91% and experiences a 3 dB scanning loss at the maximum scanning angles.

### 3.3.2 Scan Loss

Electronically steering the beam away from the boresight direction decreases the energy concentration within the main beam, which consequently lowers the antenna gain at specific angles relative to its boresight performance. This phenomenon, known as scan loss, significantly impacts the antenna's effective radiated power (ERP) and the gain-to-noise temperature ratio (G/T).

## 3.4 Phase Shifter

This element plays a crucial role in beam steering by introducing a time delay from 0 to $\lambda/c$, achieved through altering signal propagation distance or phase velocity. Progressive delay at each antenna yields constructive interference at a specific angle. PSs are classified as analog or digital. Analog offers continuous phase control for precise steering but requires DACs for voltage control. Conversely, digital phase shifters (DPS) use discrete control voltages, simplifying the control circuit at the cost of lower accuracy. Both types necessitate digital interfacing for computer control. To enable phased shifting in both transmission and reception, many phased shifters are designed to be reciprocal, facilitating bidirectional signal manipulation. [22], [6], [18].

### 3.4.1 Phase Shifter Types

The switching line PS incrementally increases phase by adding line lengths, each length corresponding to a discrete phase. Figure 3.2 demonstrates how the switches in a 3-bit DPS alter the signal path for an input of [1 1 0], resulting in a total phase shift of 270°. This type of shifter boasts rapid operation and low weight, yet suffers from perceived losses and power-handling limitations. Various switch types exist, with notable examples being the PIN diode and micro-electrcomechanical system (MEMS) [18] [6].

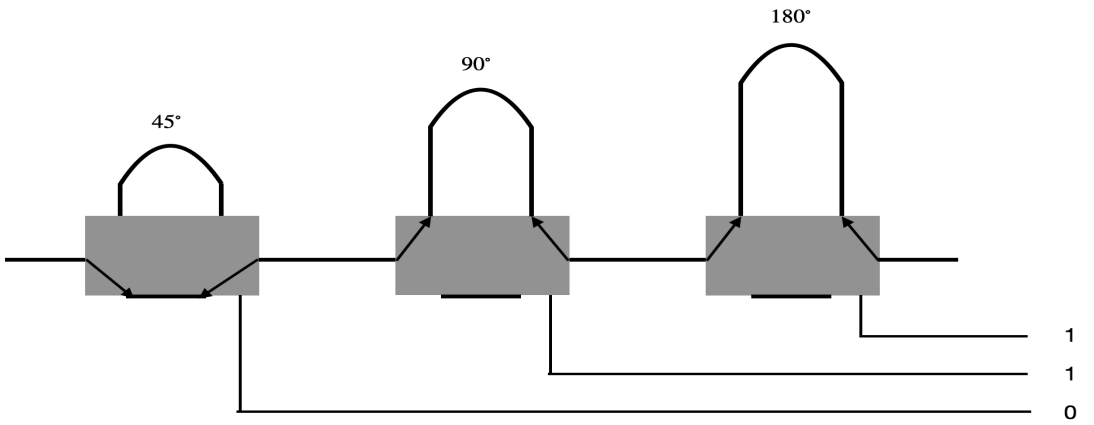


Figure 3.2: Diagram of a 3-bit switched line PS to obtain 270° phase shift 3.2

PIN diode switches are constrained by carrier lifetime, restricting their use to frequencies around 1 MHz and their current-controlled attribute is seen as a disadvantage. Meanwhile, MEMS switches stand out for their compact size, superior isolation, and linearity, in addition to their low power usage and wide frequency range. Nonetheless, at micro- and millimeter wave frequencies, MEMS switches suffer from high losses and can only handle limited power (about 100 mW). An expensive protective packaging for MEMS's bridges is required against all environ-

mental conditions. Their operation is based on applying voltage to a gate which leads to an electrical path causing analog phase shifting. Although initially prone to reliability issues, recent technological improvements have significantly boosted their dependability, positioning them as strong contenders in the switch technology arena [6].

Ferrite PSs constitute one type of device where magnetizing a ferrite element induces phase shifting. The phase shift magnitude is determined by the ferrite's length, which defines two saturation states. Within these states, the current adjusts the phase shift as needed. If the phase shift depends on the signal's path, such a PS is considered reciprocal. Another category involves Ferroelectric PSs, which incorporate ferroelectric materials in part or all of the phase shifting mechanism. The tunable dielectric constant of ferroelectric materials allows for the adjustment of the substrate's permittivity, thereby controlling the signal's phase velocity. These last two types of PSs enable phase adjustment without physically altering the signal path's length [6] [23].

Numerous circuit techniques have been innovated to enhance component performance, among which the Microwave Monolithic Integrated Circuit (MMIC) stands out due to its utilization of thin-film technology. This approach yields PSs that are not only compact in size but also characterized by low loss and an extensive phase range. Capable of achieving up to 360° of beam steering, these devices operate across a broad frequency spectrum, nearing the Terahertz region. Thanks to MMIC technology, the performance of PSs has significantly advanced, marking a notable progression in their capabilities [6] [18] [24].

### 3.4.2 N-bit Digital Phase Shifter

The phase states that DPS can offer is based on two-state phase bit. For a N-bits DPS the $n$-th bit provide a phase state $\Theta_n$ which can be calculated as follows:

$$\Theta_n = 2^n \cdot \frac{360^\circ}{2^N} \; ; \qquad n = 0, 1, 2, 3, ..., (N-1). \tag{3.13}$$

Utilizing a 3-bit DPS, the phase states that can be achieved include 45°, 90°, and 180° [18]. Table 3.1 illustrates the comprehensive list of potential phase states, each corresponding to distinct combinations of the bits.

Table 3.1: All possible phase states and the corresponding phase shift 3-bit DPS provides

| Control Bits | | | $\Theta_2$ | $\Theta_1$ | $\Theta_0$ | $\Theta_{tot}$ |
|---|---|---|---|---|---|---|
| 0 | 0 | 0 | 0° | 0° | 0° | 0° |
| 0 | 0 | 1 | 0° | 0° | 45° | 45° |
| 0 | 1 | 0 | 0° | 90° | 0° | 90° |
| 0 | 1 | 1 | 0° | 90° | 45° | 135° |
| 1 | 0 | 0 | 180° | 0° | 0° | 180° |
| 1 | 0 | 1 | 180° | 0° | 45° | 225° |
| 1 | 1 | 0 | 180° | 90° | 0° | 270° |
| 1 | 1 | 1 | 180° | 90° | 45° | 315° |

### 3.4.3 Phase Shifter Errors

Achieving a precise desired phase with PSs is limited and is instead approximated based on the number of bits in the shifter. As explained earlier an N-bit PS offers $2^N$ phase states. DPSs offer a discrete set of phase shifts, leading to a sawtooth approximation of desired values when quantizing the phase at each element as illustrated in Figure 3.3. This phenomenon is referred to as quantized lobes, and the periodicity of the triangular phase errors results in undesired sidelobes levels (SLL). Similarly, quantizing the amplitude at each antenna element is regarded as an additional source of error [20].

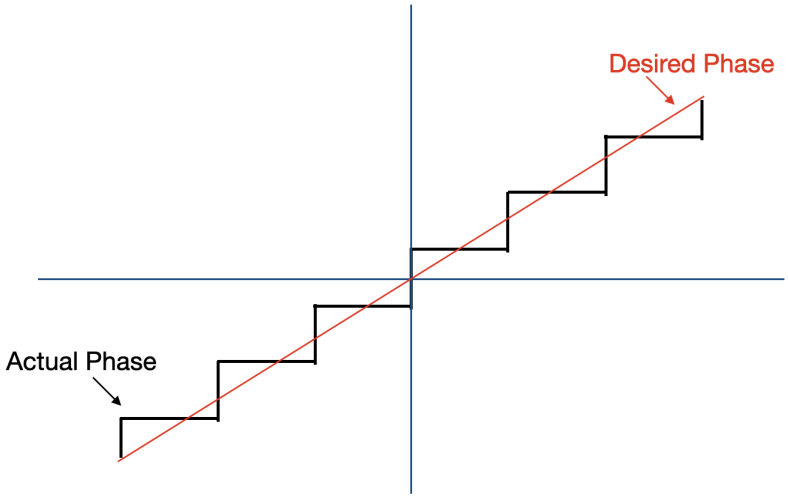


Figure 3.3: Phase quantization error [20]

### 3.4.4 Digital Phase Shifter at D-band

In a notable study on vector-sum DPSs designed for the W-band, specifically within the $90-98$ GHz range, a novel approach utilizing a 40-nm CMOS technology was introduced [25]. The design incorporates a quadrature all-pass filter (QAF) alongside four identical variable gain amplifiers (VGAs), each equipped with 7-bit current-digital to analog converters. A significant aspect of this work was addressing the

parasitic loading capacitance effect introduced by the VGAs, which was adeptly compensated for with an inductor-based compensation network. The primary objective of this innovation was to develop a 9-bit PS characterized by high phase accuracy and minimal power consumption. To further refine phase error performance, digital pre-distortion (DPD) technology was employed. This PS is distinguished by its return losses at both input and output, maintaining levels below $-10$ dB across the full bandwidth. Performance metrics revealed a peak average of $-1.29$ dB at 92.1 GHz, with RMS amplitude and phase errors ranging between $0.67 - 1.23$ dB and $0.6° - 0.7°$, respectively, throughout the bandwidth. Notably, the minimum RMS amplitude error was recorded at 0.67 dB at 93.4 GHz, and the lowest RMS phase error was 0.60° at 94.1 GHz. The input and output 1 dB compression points ($P_{1dB}$) were measured at $-7.11 \pm 1.44$ dBm and $-9.47 \pm 1.65$ dBm, respectively, while the NF varied from 7.92 to 12.31 dB across the bandwidth. The PS operates with an efficiency of 14 mW from a 1.1 V supply [25].

## 3.5 Attenuator

The attenuator, also known as the amplitude control circuit, is a two-port device primarily designed to reduce power levels. Commonly utilized across various applications, including impedance matching and managing the output power of amplifiers, attenuators achieve the desired output power by dissipating a portion of the input power as heat. This dissipation process must be managed carefully to prevent overheating. A fundamental type of attenuator uses a lossy transmission line to absorb power, with the line's length directly influencing the amount of power dissipated. However, a limitation of this approach is the requirement for very long transmission lines to achieve significant power attenuation. An alternative attenuation method involves reflecting a portion of the input power. Among the most prevalent types of attenuators are those comprising resistors, which are insignificant in size relative to the wavelength. In these devices, the degree of attenuation is determined by the specified resistive values of the resistors [20], [6], [26].

Within a phased array transceiver system, the attenuator is regarded as a crucial component due to its multifaceted role in gain control. It is utilized for compensating amplitude fluctuations, managing gain, and performing tapering actions to diminish the intensity of unwanted sidelobes. For mmW applications, a variety of attenuator designs have been introduced, capable of offering discrete levels of power attenuation, often referred to as digital attenuators. These include distributed attenuators, differential $\pi$-type attenuators, reflective attenuators, and Radio Frequency Micro-ElectroMechanical Systems (RF-MEMS) attenuators [27], [28], [29].

### 3.5.1 Quantisation Error of Digital Attenuator

Acquiring exact analog values with digital components, like PS or attenuators, results in approximations to the closest digital equivalent. Unlike PS, the precision of an attenuator's least significant bit (LSB) is not strictly tied to its bit count but rather to its design, meaning a higher bit count doesn't automatically ensure finer

resolution. The attenuation offered by an N-bit attenuator can be expressed as a sequence starting from the least significant bit (LSB) value and doubling it sequentially for each additional bit, leading up to $LSB \times 2^N$. This formula captures the range of attenuation levels that such an attenuator can provide, illustrating how the resolution and maximum attenuation are influenced by the attenuator's LSB. The formula for calculating a N-bit attenuator's maximum attenuation is:

$$Attenuation_{max}[dB] = (2^N - 1)LSB_{dB}. \tag{3.14}$$

For example, a 6-bit attenuator with a 0.5 dB minimum step can achieve up to 31.5 dB of attenuation [30]. In contrast, a 5-bit attenuator with the same step size reaches a maximum of 15.5 dB [29]. Opting for a smaller LSB reduces quantization errors and in turn, enhances the performance.

### 3.5.2 Attenuator at W-band

In the study referenced as [29], a reflective-type attenuator was developed and evaluated for operation within the W-band, specifically across frequencies ranging from 70 to 110 GHz. The design structure of this attenuator, as presented in 3.4, primarily consists of a quadrature coupler and two identical resistive loads. Through various modifications aimed at enhancing performance, the attenuator demonstrates improved insertion loss and dB-linear gain tuning capabilities when compared to traditional reflective-type attenuators [29].

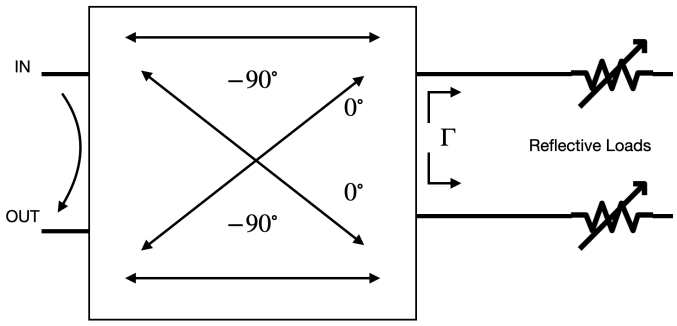


Figure 3.4: Reflective type attenuator topology [29]

Experimental results indicate that the device achieves a gain coverage of 15.5 dB with fine granularity of 0.5 dB steps, while maintaining an RMS gain error of less than 0.2 dB across the entire frequency spectrum under consideration. Additionally, the insertion loss measured falls between 3.0 and 3.8 dB throughout this frequency range. It was observed that the RMS phase error tends to increase with frequency. Furthermore, the measurement results highlights the device's ability to maintain consistent attenuation levels, displaying flat attenuation curves across the $70 - 110$ GHz band. This characteristic is particularly advantageous, as it ensures nearly uniform attenuation performance regardless of the operating frequency [29].

## 3.6 Low Noise Amplifier

The low noise amplifier (LNA) stands as a pivotal element in the receiver chain, positioned immediately after the antennas. Its primary role is to enhance the power of the incoming weak signals while minimally affecting their signal-to-noise ratio (SNR). Several key parameters are crucial when evaluating an LNA to ensure it meets the specific needs of the system. Among these, the noise figure (NF) is paramount, as it essentially sets the system's noise performance based on the LNA's characteristics. Noise in electrical devices makes signal detection challenging, particularly for receivers that pick up noise from various sources along with the intended signal. Unlike transmitters, where the emphasis is on gain and power, receivers require careful attention to the noise figure. To ensure reliable signal detection, the receiver's noise floor, or the ambient noise power, must be minimized and kept below the power of the received signal [31]. The NF is defined as the ratio of the output noise temperature $T_{out}$, which includes the input noise at temperature $T_0$ amplified by the gain, plus the internally generated noise $T_{int}$, to the output noise temperature $T_{out}$ [32], [20]. Consequently, the NF can be formulated as follows:

$$NF = \frac{T_{out} + T_{int}}{T_{out}} = \frac{G \cdot T_0 + T_{int}}{G \cdot T_0}. \tag{3.15}$$

Maintaining the operation of the LNA within its linear region is crucial to prevent undesirable outcomes, with the 1-dB compression point serving as a key indicator for this purpose. Essentially, a linear amplifier maintains a consistent gain, meaning the output power directly corresponds to the input power. This characteristic is vital in communications to avoid signal distortion, which non-linear amplifiers can introduce, thereby impairing performance. 1-dB compression point marks the input power level at which the gain drops by 1 dB from its linear behavior, signaling the onset of nonlinearity; amplifiers typically function normally below this threshold. In the context of phased array systems, it is essential for the LNA to demonstrate consistent gain and phase stability across a defined temperature range and throughout its operational lifespan. This stability is critical for beamforming applications, as significant deviations can adversely affect the formation and direction of the desired beam [32], [6].

Given the high value placed on LNA with minimal NF, efforts have been directed towards advancing transistor technologies that contribute to LNA efficiency. Three principal technologies, all variations of the high-electron-mobility transistor (HEMT) paradigm, have been utilized. These include the use of gallium-arsenide (GaAs) and/or indium-phosphide (InP) compound semiconductors, with InP known for its superior low NF characteristics. The foundational technology among these is the conventional field-effect HEMT. Progress in this field led to the development of the pseudomorphic HEMT (pHEMT), offering enhanced performance. The most advanced iteration in this technological evolution is the metamorphic HEMT (mHEMT), representing a further refinement in achieving lower noise figures and improving LNA performance [32].

### 3.6.1 LNA at W-band

In a significant contribution to the field of LNA, a study outlines the design and fabrication of an LNA operating within the $80-122$ GHz range, utilizing 70-nm GaN HEMT technology for MMIC implementation. The primary aim of this research was to create a wideband LNA that harmonizes a low NF with high output power, leveraging a meticulously optimized three-stage low-noise input stage paired with a two-stage output core configured in a balanced arrangement. The resulting amplifier demonstrates an NF ranging from 3.5 to 5.5 dB and a saturated output power ($P_{sat}$) between 22.8 and 24.3 dBm. Impressively, the gain ($S_{21}$) surpasses 24 dB across a broad spectrum from 76 to 122 GHz, while maintaining an input return loss below $-8$ dB and an output return loss below $-20$ dB over the 90 to 110 GHz frequency range. Furthermore, within this specified bandwidth of 20 GHz, $P_{1dB}$ spans from 26.5 to 29 dBm, with an efficiency rate of $5-8$ % observed [33].

## 3.7 Power Amplifier

Power amplifiers (PA) play a crucial role in the transmitter chain, where they are positioned at the final stage. Their primary function is to boost the signal power to the necessary level for successful transmission, ensuring effective communication [20]. When designing PAs, one of the paramount criteria is linearity. The linearity of an amplifier, as mentioned earlier in 3.6, is often gauged by the 1 dB compression point, indicating the threshold beyond which the input and output power no longer maintain their linear relationship. Given that the fundamental objective of a PA is to enhance the signal's input power, the output power and the amplifier's efficiency are also key factors in determining its quality [31]. PAs that achieve a given output power while consuming less DC power are considered more efficient. This efficiency is measured as the ratio of the output signal power to the input DC power. Just as with LNA, achieving minimal gain variation across the desired bandwidth is an important consideration in the design of PAs. [34].

The push for broader bandwidths and enhanced performance of mmW amplifiers operating at higher frequencies has driven continuous advancements in transistor technologies. This shift in focus from traditional traveling wave tubes (TWT) and klystron amplifiers, which remain prevalent in radar technologies, to solid-state PAs is due to the latter's superior performance at higher frequencies. Silicon's affordability and the ability to grow high-quality dielectric materials on it for insulation have led to the predominance of Silicon semiconductors in the market. Technologies like Complementary Metal-Oxide-Semiconductor (CMOS) and Bipolar CMOS (BiCMOS) are foundational to these transistors, offering high-frequency amplifiers with excellent characteristics [31] [35].

### 3.7.1 Power Amplifier at D-band

In the study conducted on PA designs based on SiGe BiCMOS technology, two configurations were analyzed: a single-ended amplifier and a differential amplifier,

both targeted to operate with a large bandwidth centered at 135 GHz. The primary aim of this research was to improve the linearity of these amplifiers. The differential amplifier, in particular, demonstrated superior performance, with an $S_{21}$ parameter exceeding 18 dB across the frequency span of 125 to 150 GHz, thereby ensuring stability throughout its bandwidth. It achieved a 1 dB compression point ($P_{1dB}$) of 18.5 dBm and a saturation power of 19.3 dBm, both at the central frequency. Moreover, the differential amplifier's $P_{1dB}$ exceeded 17 dBm, with its power efficiency surpassing 11% over a frequency range from 125 GHz to 140 GHz. The input and output return losses remained below $-14$ and $-5$ dB between 120 GHz and 140 GHz respectively, indicating an effective impedance match. Although the differential amplifier outperformed the single-ended version in most respects, including stability and linearity, the latter did achieve a maximum gain of 24 dBm and exhibited commendable power efficiency [36].

## 3.8 Band-Pass Filter

Another crucial component in wireless communication systems is the filter, which is characterized by several key performance properties. The first is the attenuation of the input signal in the passband; ideally, this should be minimized, a characteristic known as low passband insertion loss. Another important attribute is the size of the filter, which should be compact, coupled with a large bandwidth. Band-pass filters are designed to permit only a specific range of frequencies to pass through while blocking or significantly reducing the amplitude of frequencies outside this range. In [37], a compact interdigital band-pass filter (iBPF) with size of $0.24 \times 0.7$ mm$^2$ and centered at 95.5 GHz is designed. It achieves a bandwidth of 40 GHz, with the $S_{11}$ parameter remaining below -30 dB across the entire bandwidth.

## 3.9 Uncertainty Sources

Achieving theoretical results can be challenging due to various sources of uncertainty that affect performance. Signal transmission through an electrical device experiences degradation due to reflections at component interfaces, and impedance mismatches between these components lead to deviations in amplitude and phase. Additionally, mechanical manufacturing errors often cause component deformation, altering signal path lengths, leading to amplitude and phase discrepancies. Temperature changes significantly impact performance, alongside aging and mutual coupling as additional uncertainty factors. This study primarily examines phase fluctuations in active RF components caused by mechanical errors and temperature variations, focusing on high-frequency components where such effects on amplitude excitation are considered minimal. The sources of errors in antenna array systems can be broadly classified into systematic and random types. Systematic errors, which are deterministic in nature, can often be predicted with theoretical analysis or identified through empirical measurements. This implies that components produced using the same

electrical design and manufacturing processes will exhibit consistent errors. Thus, the calibration methods proposed in this study aim to address these systematic discrepancies. However, even with systematic error calibration, achieving performance perfectly aligned with theoretical predictions is hindered by random errors, which introduce unavoidable variations. These variations necessitate the use of statistical analysis to evaluate their impact on system performance, emphasizing the inherent challenges in aligning practical outcomes with theoretical ideals [38] [39] [40].

### 3.9.1 Multiple Reflections

A wave propagating through an electrical device undergoes reflection and transmission at the interfaces. Merely accounting for these phenomena at each interface singularly is insufficient for comprehensively understanding the overall reflection. Consider a scenario where a normally incident wave traverses a device (described as a "black box" with width $d$), moving from medium 1 into medium 3, as depicted in Figure 3.5. At interface 1, $\Gamma_{12}$ refers to the reflected wave, while $T_{12}$ refers to the portion of the wave that continues through the device. Upon reaching the second interface, after traveling a distance $d$, a segment of the wave transmits into medium 3, and the remainder reflects back towards the first interface, represented in $T_{23}$ and $\Gamma_{23}$, respectively. A fraction of the latter reflected wave at interface 1 then transmits into medium 1, with the residual wave reflecting within the device, and so on as illustrated in Figure 3.5. To put it more succinctly, the reflected wave at the first interface embodies the aggregate of reflected signals through the device and the total coefficient reflection can be calculated as follows:

$$\Gamma_{total} = \frac{\Gamma_{12} + \Gamma_{23} e^{-2\gamma_2 d}}{1 + \Gamma_{12}\Gamma_{23} e^{-2\gamma_2 d}} \tag{3.16}$$

while the total transmission coefficient is expressed as follows:

$$T_{total} = \frac{T_{12} T_{23} e^{-\gamma_2 d} e^{\gamma_3 d}}{1 + \Gamma_{12}\Gamma_{23} e^{-2\gamma_2 d}} \tag{3.17}$$

where $\gamma$ is the propagation constant and can be obtained as follows:

$$\gamma = \sqrt{j\omega\mu(\sigma + j\omega\epsilon)} \tag{3.18}$$

where $\omega$, $\mu$, $\epsilon$ and $\sigma$ are the angular frequency, relative permeability, relative permittivity and conductivity of a material, respectively [41].

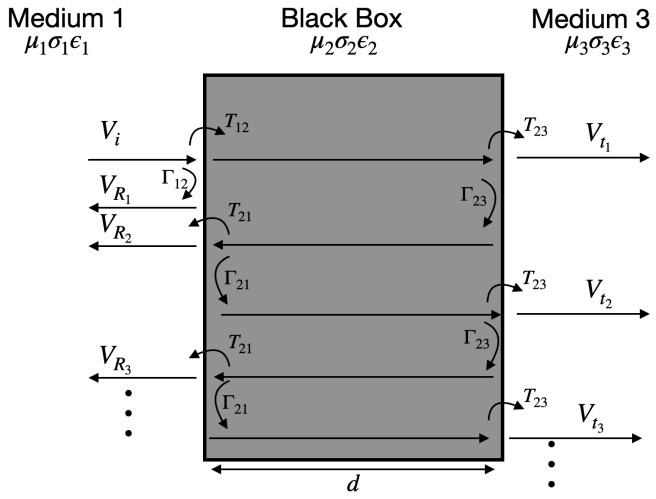


Figure 3.5: Multiple reflection within black box [41]

### 3.9.2 Missmatch Loss Uncertainties

Figure 3.6 illustrates the propagation of the signal $V_i$ from a source with impedance $Z_s$ through a transmission line of length $l$ and characteristic impedance $Z_0$, reaching a load with impedance $Z_l$. If the impedance of the transmission line does not match the load impedance ($Z_l \neq Z_0$), a portion of the incident wave at the load, $V_{RL}$, is reflected back towards the source. Similarly, if the source impedance $Z_s$ does not match the transmission line's impedance $Z_0$, a part of $V_{RL}$ is further reflected back at the source, denoted as $V_{RS}$. Consequently, the reflected signal $V_{RS}$ combines with the incident wave $V_i$, introducing amplitude and phase uncertainties based on $V_{RS}$'s characteristics. These uncertainties manifest as amplitude and phase ripples, which are determined by the reflection coefficients of the source and load, $\Gamma_s$ and $\Gamma_L$, respectively. The amplitude deviation $\Delta_{amplitude}$ falls within the bounds of positive and negative amplitude uncertainty, which can be mathematically represented in dB according to [35] as follows:

$$\Delta_{amplitude-dB} = 20 \cdot \log(1 \pm |\Gamma_S| \cdot |\Gamma_L|) \tag{3.19}$$

while the phase deviation $\Delta_{phase}$ can be obtained as below:

$$\Delta_{phase} = \pm \tan^{-1}(|\Gamma_S| \cdot |\Gamma_L|) \tag{3.20}$$

.

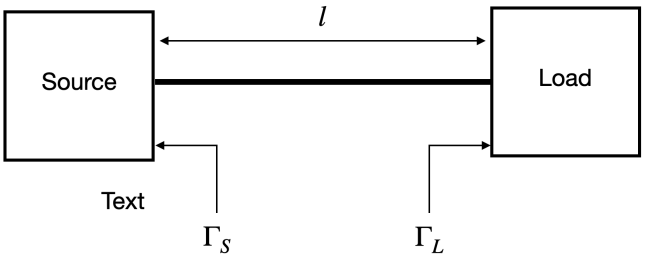


Figure 3.6: Signal reflection due to impedance mismatch between load and source [35]

Figure 3.7 depicts the superposition of the incident vector $V_i$ with its rereflected counterpart $V_{RS}$. The frequency spacing between the peaks of the ripples is determined by twice the propagation distance of the wave combined with the signal's wavelength, represented as $c/2l\sqrt{\epsilon_r}$ where $\epsilon$ is the relative permeability [35].

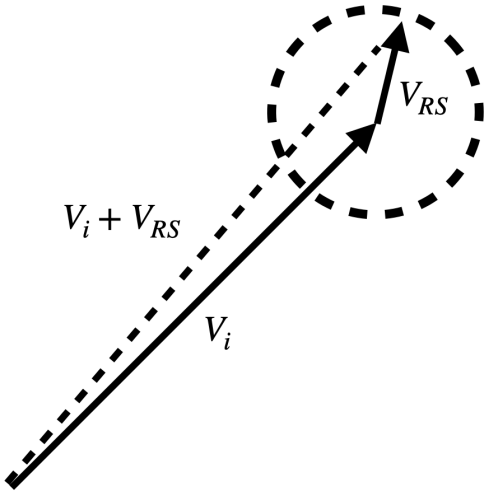


Figure 3.7: The total vector is the sum of the incident wave $V_i$ and the rereflected wave $V_{RS}$ [35]

### 3.9.3 Mechanical Errors

During manufacturing, various mechanical errors can arise, with some predictable through theoretical analysis and others identifiable only via empirical measurements. The study in reference [42] explores two distinct kinds of structural distortions in planar rectangular phased array antennas through deterministic analysis. The first kind, termed "bent slab" or single curvature, involves the planar phased array's ends bending upward, as illustrated in Figure 3.8a. This distortion, assuming the antenna is positioned in the xy-plane, affects the z-direction, necessitating the inclusion of an additional phase factor to the array's total electrical field and 3.7 can be rewritten

as follows:

$$E(\theta,\phi)_{total} = \sum_{m=1}^{M}\sum_{n=1}^{N} E_{m,n} I_{m,n} e^{(j(m-1)(n-1)(kd(\sin\theta\cos\phi+\sin\theta\sin\phi)+\psi_{m,n}+kz_{m,n}\cos\theta))} \tag{3.21}$$

where $z_{m,n}$ denotes the displacement factor and can be expressed as follows:

$$z_{m,n} = z_{max}(\frac{x_{m,n}}{x_{max}})^2. \tag{3.22}$$

Here $z_{max}$ is the maximum displacement in the z-direction, $x_{max}$ is half of the array length in the x-axis and $x_{m,n}$ is the position of the $[m,n]$-th array element in the x-axis. This modification is critical for accurately representing the antenna's electrical behavior under such distortion.

The author in [42] explores another mechanical distortion termed Double-Curvature or Bow Distortion, which alters the central section of a planar array into a bowl-like shape while its periphery remains unchanged as shown in Figure 3.8b. Though the electric field's formula due to this particular distortion remains as outlined in 3.21, the equation to describe the displacement resulting from Bowl Distortion is provided as:

$$z_{m,n} = z_{max}\left(1-(\frac{x_{m,n}}{x_{max}})^2\right)\left(1-(\frac{y_{m,n}}{y_{max}})^2\right) \tag{3.23}$$

where $y_{max}$ is the half length of the array antenna in the y-direction and $y_{m,n}$ is the position of the $[m,n]$-th element in the y-axis. Thus the phase shifts to compensate for these errors can expressed as follows:

$$\Phi_{m,n} = e^{-jk\cos\theta_0 z_{m,n}}. \tag{3.24}$$

Not all mechanical errors can be precisely predicted through analytical methods, making it essential to perform physical measurements of the antenna and implement calibration algorithms. In this study, we focus exclusively on the analysis of bent slab distortion.

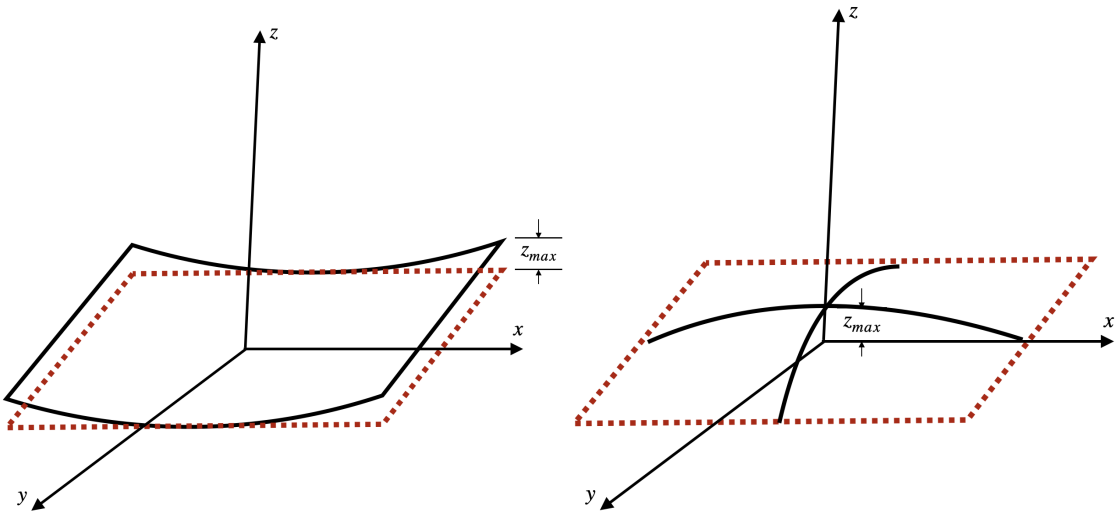


(a) Bent Slab (b) Bowl Distortion

Figure 3.8: Structure distortion due to mechanical error [42]

### 3.9.4 Temperature Drift

Temperature impacts on antenna performance are a critical focus in antenna calibration, as transmitter/receiver chains must operate effectively across various temperatures influenced by ambient conditions, solar exposure, and component heating from devices such as amplifiers [43] [44] [45]. The electrical components within these chains are particularly temperature-sensitive, which can lead to performance degradation. Therefore, it is essential to assess the effects of temperature and integrate this understanding into the calibration process to address potential performance impairments caused by temperature fluctuations. Temperature-related degradation manifests in two main ways. Firstly, port excitation drift occurs due to thermal drift, which results in amplitude and phase deviations, leading to performance degradation.

The references [44] and [43] describe how the gain and phase insertion in both modules linearly vary with temperature. For instance in [44] the amplitude and phase degrade approximately at the rate of 0.016 dB/°C and 0.6 deg/°C respectively. In [46], formulas are derived for amplitude and phase errors across a temperature range from -80°C to 100°C, based on experimental testing of TX/RX modules. The errors for the amplitude and phase of the [m,n]-th element, $\Delta I_{m,n}$ and $\Delta\psi_{m,n}$, in an M×N element array are determined as outlined in [46]:

$$\Delta I_{m,n} = \begin{cases} 1.27^{\frac{T+40}{5}} - 0.124 & -80° \leq T < -40° \quad (3.25a) \\ 0.002T + 0.959 & -40° \leq T < -20° \quad (3.25b) \\ 0.99 & 20° \leq T < 30° \quad (3.25c) \\ -0.00179T + 1.0536 & 30° \leq T < -86° \quad (3.25d) \\ 0.5^{\frac{T-86}{6}-0.15} & 86° \leq T \leq 100°. \quad (3.25e) \end{cases}$$

$$\Delta\psi_{m,n} = \begin{cases} -0.00016T^2 - 0.03408T + 3.09 & -80^\circ \leq T < -30^\circ \quad (3.26a) \\ 0.0008T^2 - 0.025T + 2.5 & -30^\circ \leq T < 0^\circ \quad (3.26b) \\ \dfrac{-1}{130T} + 2.5 & 0^\circ \leq T < 26^\circ \quad (3.26c) \\ 2.3 & 26^\circ \leq T < 50^\circ \quad (3.26d) \\ 0.03T + 0.8 & 50^\circ \leq T < 70^\circ \quad (3.26e) \\ 2.9 & 70^\circ \leq T \leq 100^\circ. \quad (3.26f) \end{cases}$$

This project adopts the deviations in amplitude and phase as specified in the formulas above and uniform temperature distribution across the array element is assumed. The influence of temperature drift on phase and amplitude distribution is critical and warrants thorough investigation and calibration.

Secondly, thermal deformation of the antenna structure alters the radiation pattern characteristics, causing deviations from the expected theoretical performance [47] [48]. The linear deformation of length L due to change in temperature $\Delta T$ can be expressed as follows [47]:

$$\Delta L = \alpha L \Delta T \tag{3.27}$$

where $\alpha$ is the thermal expansion coefficient. This deformation results in alterations to the spacing between the elements of the array.

# 4

# Method

## 4.1 Calibration Method

Numerous literature studies have explored the phase and amplitude calibration of phased array antennas at lower frequencies. This thesis will delve into some of these algorithms to assess their applicability beyond 100 GHz. The proposed algorithms will be simulated and implemented using Matlab software. Calibration is required in both receiving and transmitting modes, and a portion of this thesis will extensively investigate the hardware fluctuations at high frequencies and their implications for the calibration process. Furthermore, a segment of the literature review will be dedicated to understanding the temperature effects on hardware components and the quantization errors arising from PSs.

As previously mentioned, OTA calibration methods are less complex as they calibrate the entire system, eliminating the need to calibrate the signal in each RF branch. Calibration processes involve measuring the antenna, and these methods are categorized based on the measurement techniques employed. Far-field measurement-based methods are often preferred because they are less sensitive to the radiation pattern, and the measurement setup has minimal impact on the results. Given the focus on higher frequencies and the resulting smaller antenna sizes, meeting far-field criteria is not a significant challenge.

Among the earliest, if not the first, calibration methods is the on/off method [49], recognized as a benchmarking algorithm in this report. Various algorithms utilizing far-field measurements have been developed, including the Rotating Element Electric Field Vector (REV) method, Fast Amplitude-Only Calibration method, and Complex Amplitude Calibration method. These approaches all necessitate only one probe antenna to complete the setup [12] [49] [50] [51]. In the [52] study, a backward transform is employed on near-field measurements for precise fault identification. Meanwhile, in [53], code division multiple-access (CDMA) is implemented based on near-field measurements for fast and accurate calibration. This section will elaborate on the benchmarking process and one additional algorithm employed for calibrating the phase and amplitude of a phased array antenna.

### 4.1.1 ON/OFF Method

Essentially, a single element of AUT receives a signal from a probe positioned at least at the Fraunhofer far-field distance from the AUT, with the remaining elements turned off. This process is repeated M times for all AUT elements, recording the frequency responses using a Vector Network Analyzer (VNA). Simultaneously, the initial excitation of the probe is stored for subsequent comparison with the recorded responses[49], [54]. It's important to note that this explanation pertains to the receiving mode, where the AUT is receiving the signal. The transmitting mode follows a similar procedure, with each AUT element transmitting the signal in each iteration, received by the probe. The comparison is once again facilitated using a VNA.

### 4.1.2 REV

In the REV method, the probe measures the composite radiated power of all AUT elements when the phase of only one element is set to a value between 0 and 360, while the others have a zero phase. This sequential calibration process is applied to all AUT elements. The composite field can be expressed as follows:

$$\dot{E} = (E_0 e^{j\theta_0} - E_n e^{j\theta_n}) + E_n e^{j\theta_n + \Delta} \tag{4.1}$$

where $E_0$ and $\theta_0$ denote the amplitude and the phase of the composite field vector at the initial states and $E_n$ and $\theta_n$ are the same for the $n-th$ element, respectively and $\Delta$ is the phase variation of the same element [51].The authors in [51] define the relative amplitude $k$ and phase $X$ as follows:

$$k = \frac{E_n}{E_0} \tag{4.2}$$

$$X = \theta_n - \theta_0 \tag{4.3}$$

. And the relative power of the composite field can be written according to [51]:

$$\frac{|\dot{E}|^2}{E_0^2} = (Y^2 + k^2) + 2kY\cos(\Delta + \Delta_0) \tag{4.4}$$

where

$$Y^2 = (\cos X - k)^2 + \sin^2 X \tag{4.5}$$

$$\tan \Delta_0 = \frac{\sin X}{\cos X - k} \tag{4.6}$$

.

Clearly the maximum power in 4.4 can be achieved when $\Delta = -\Delta_0$. The ratio of the maximum and minimum power can be expressed as follows:

$$r = \pm\frac{(Y+k)^2}{(Y-k)^2} \tag{4.7}$$

. Therefore the relative amplitude and phase can be obtained based on the sign of $r$. In case $r$ is positive we have:

$$k_1 = \frac{\Gamma}{\sqrt{1 + 2\Gamma \cos \Delta_0 + \Gamma^2}} \tag{4.8}$$

$$X_1 = \tan^{-1}(\frac{\sin \Delta_0}{\cos \Delta_0 + \Gamma}) \tag{4.9}$$

and when $r$ is negative we got:

$$k_2 = \frac{1}{\sqrt{1 + 2\Gamma \cos \Delta_0 + \Gamma^2}} \tag{4.10}$$

$$X_2 = \tan^{-1}(\frac{\sin \Delta_0}{\cos \Delta_0 + 1/\Gamma}) \tag{4.11}$$

where

$$\Gamma = \frac{r-1}{r+1}. \tag{4.12}$$

Three methods have been discussed for identifying the correct solutions. The first method involves rotating the element vector by adjusting the phase and determining the solution based on the phase change of the composite field. If this phase change is less than 180°, then $k_1$ is selected; otherwise, $k_2$ is chosen. This approach requires knowledge of both the phase and amplitude of the composite field. The second method operates by using two different initial states, each yielding a set of solutions. The correct set is identified as the one where the value of $ke^{jX}$ remains consistent. Due to measurement errors, increasing the number of initial settings is necessary to accurately discern the correct solution. The third method sets the initial composite vector such that $k < Y$ always holds, leading to the selection of $k_1$. This method is viable only when none of the elements exhibit extremely large amplitudes.

The bit-number of the PSs is a crucial factor in this method. Higher accuracy is achieved with a greater bit-number, as PSs with more phase states contribute to more precise results. However, it's important to note that this improvement in accuracy comes at the cost of increased time consumption due to the necessity for more iterations.

### 4.1.3 Modified REV

Due to a broad error range and limited accuracy in power measurement, the traditional REV might incorrectly add $\pi$ when the phase associated with maximum power $\Delta_0$ is close to $\pm\pi/2$.In simpler terms, the arctan function used in traditional REV provides a value within the range of $\pm\pi/2$. However, the correct phase range spans the entire $2\pi$, necessitating the addition of $\pi$ depending on $\Delta_0$. Figure 4.1 illustrates that while $\Delta_0$ is positioned at $\pm\pi/2$, the phase that yields maximum power actually lies just outside this range, very close to $\pm\pi/2$. This close proximity calls for the addition of $\pi$ to align with the true phase position. However, REV often opts not to make this adjustment, which results in $\pi$ error. Consequently, a modified

version of REV is introduced in [55]. This version follows a similar procedure to the traditional REV, beginning with adjusting the phase of one element from 0° to 360° in the smallest increments allowed by the PS to identify the phase shift, $\Delta_0$, that corresponds to the maximum power. However, unlike the traditional REV, the modified REV sets $\Delta_0$ at the first element before proceeding to calibrate the subsequent elements, continuing this process through all elements. This approach eliminates the $\pi$ uncertainty and does not depend on exact measurements of maximum and minimum power.

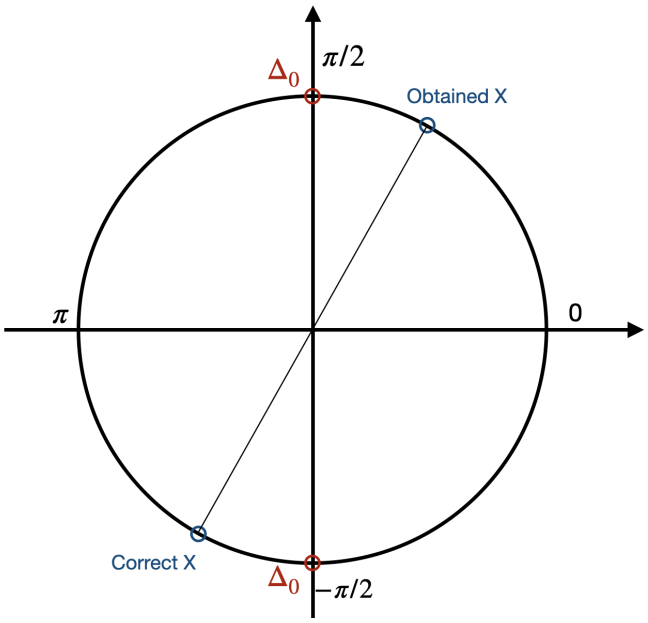


Figure 4.1: $\tan^{-1}$ function return values in range of $\pm\pi/2$ and REV mistakenly gives the wrong phase shift when $\Delta_0$ is very close to $\pm\pi/2$.

## 4.2 Calibration Setup

Reference [21] indicates that the maximum size of an array antenna operating at 100 GHz, denoted as $D$, is 2 cm. This implies that the minimum required distance for far-field measurements is $\frac{2D^2}{\lambda} = 0.3$ m. Consequently, this requirement can be met within a compact anechoic chamber, making it an ideal choice as it ensures line of sight measurements without necessitating a large and costly chamber. This report examines two modules: the transmission module, where the AUT functions as the transmitter, and the receiving module, where the AUT serves as the receiver. The setup for both modules is similar, as depicted in figure 3.1, utilizing a VNA to compare the predefined signal transmitted/received by the probe antenna with the signal received/transmitted by the AUT. A laptop controls the PSs and attenuators within the black box, besides executing calibration algorithms. Figure 4.2 presents the schematic of the black box applicable to both modules, with the distinction that a LNA is employed in the receiving module and a HPA in the transmitting module. The remaining components—comprising the filter, the PS, and the atten-

uator—remain consistent across both setups.

The slot array described in [21] features a center-fed design with the feed point located at the antenna's edge, resulting in a transmission line within the antenna that is 1 cm long through which the signal propagates. It is assumed that the transmission line connecting the antenna to the black box matches the length of the internal antenna transmission line. Within the black box, the distances between components, as well as from the components to the black box's edge, are assumed to be 0.5 cm. These design choices are informed by various studies [56] [57] [58] on transceiver design in this frequency range, where the objective has been to maintain compact dimensions while accommodating the tolerances of milling machines. Essentially, the goal is to minimize the length of the transmission line to reduce signal losses and the standing-wave ripple, but practical manufacturing limitations necessitate a balance between compactness and feasibility.

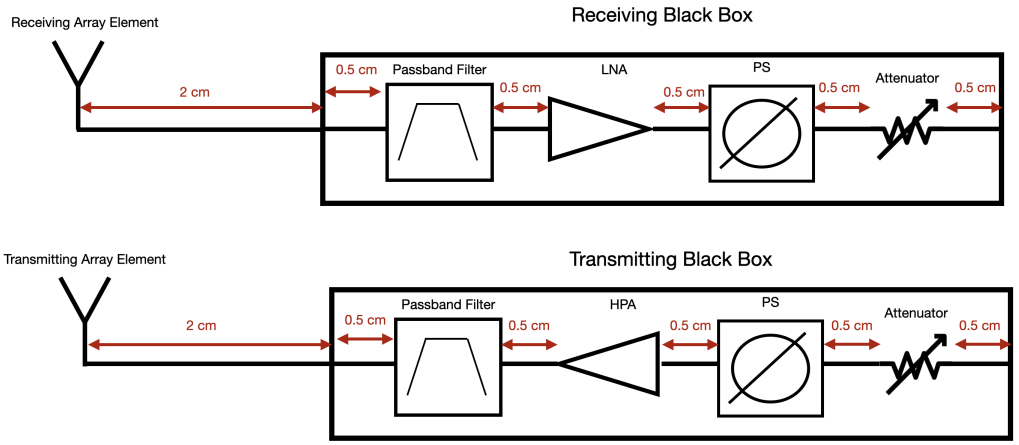


Figure 4.2: Block diagram of the transmission and receiving modules with the antenna, highlighting the specified lengths of the transmission lines.

## 4.3 Beam Book

In this study, the antenna is designed to cover angles ranging from $-60°$ to $+60°$. To ensure comprehensive coverage, calibration must be conducted at various angles within this range. The necessary beams for achieving the desired coverage with a specific antenna are documented in what is known as a "beam book." This resource is invaluable for identifying which beams require calibration and for recording calibration data, which can then be used to calibrate similar antennas. The density of calibration intervals in the beam book depends on the necessary gain. For example, it might be essential to maintain a minimum gain within the target range. As long as the gain exceeds the stipulated threshold in any direction, it is deemed satisfactory. Alternatively, achieving specific gain levels at certain angles may be crucial, depending on the antenna's application. This requires that the gain at any crossover point between adjacent beams should not drop below a critical threshold for key angles within the operational range. Increasing the number of elements in

a phased array antenna results in a narrower beamwidth, necessitating more dense calibration to achieve the desired performance. In this study, the beam book for the 8-element array is set at [−58°, −36°, −18°, 0°, 18°, 38°, 56°]. This setup aims to mimic the radiation pattern illustrated in Figure 4.4, with a defined threshold of 24 dBi. In contrast, the 4-element array, which offers a wider beamwidth and the threshold is set at 18 dBi, the corresponding beam book consists of angles of [−60°, −23°, 13°, 53°]. This arrangement seeks to recreate the radiation pattern shown in Figure 4.3. The rationale for selecting these thresholds is to ensure a minimum margin of 1.4 dBi at points where the beams intersect and along the boundaries of the targeted coverage area, specifically at ±60°.

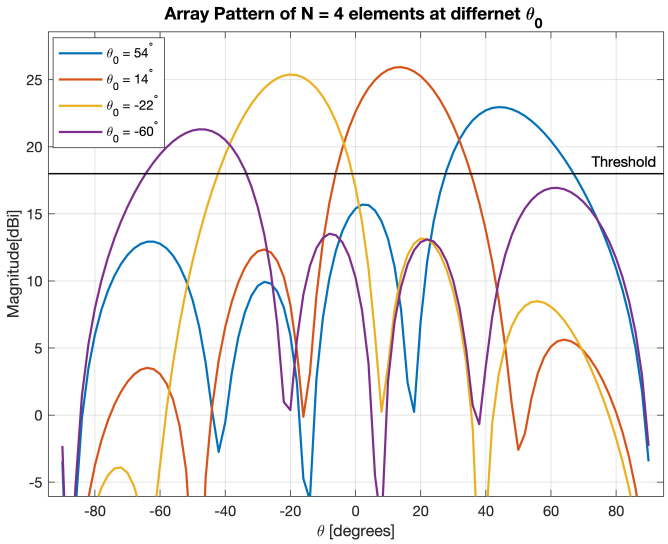


Figure 4.3: Beam book for a 4-element array designed to achieve coverage of ±60° with a threshold set at 18 dBi.

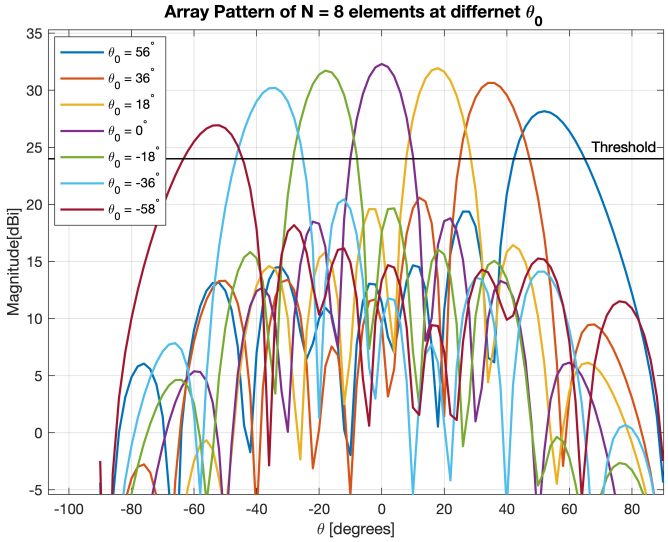


Figure 4.4: Beam book for a 8-element array designed to achieve coverage of ±60° with a threshold set at 24 dBi.

### 4.3.1 Enhanced Beam Book

The beam books shown in figures 4.3 and 4.4 are calibrated across all beams to maintain gains above a predetermined threshold. An alternative strategy involves increasing the number of beams in each beam book while calibrating fewer of them, thereby reducing both calibration time and effort. For instance, in the 4-element array, rather than calibrating four beams, the enhanced beam book presented in figure 4.5 now includes five beams positioned at [−60°, −28°, 0°, 26°, 60°], with only the beams at −60°, 0°, and 60° are calibrated. Similarly, the enhanced beam book for the 8-element array, illustrated in figure 4.6, features beams at [−58°, −42°, −30°, −15°, 0°, 15°, 30°, 42°, 56°], with beams at [−58°, −30°, 0°, 30°, 56°] being calibrated.

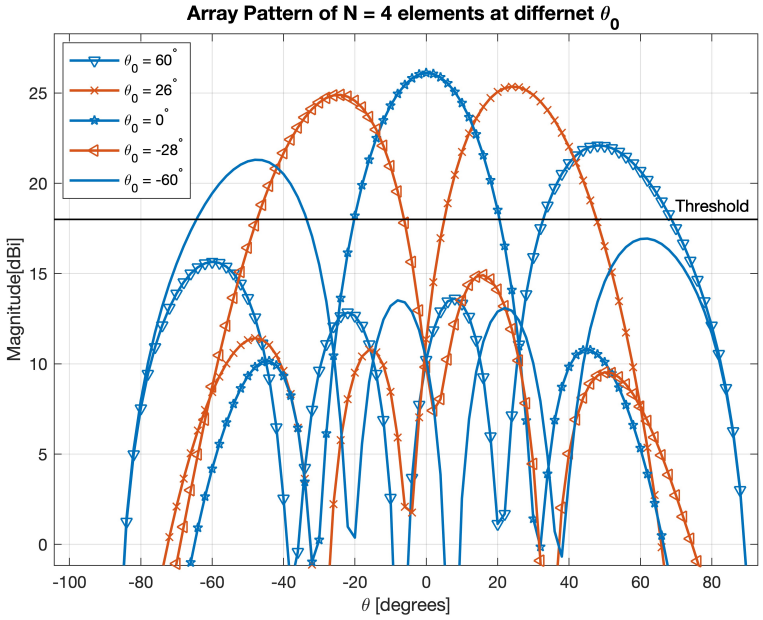


Figure 4.5: Enhanced beam pattern of a 4-element array showing calibrated beams at -60°, 0°, and 60° in blue, while the uncalibrated beams are depicted in red.

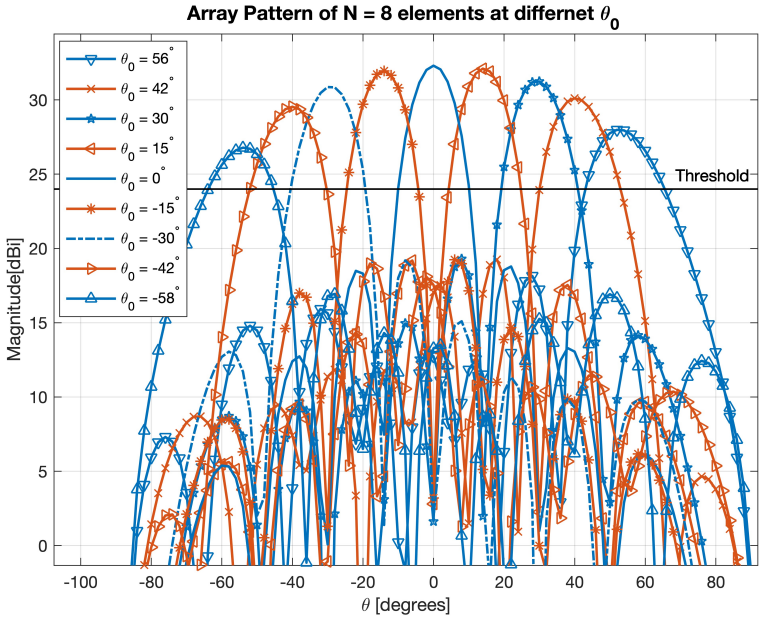


Figure 4.6: Enhanced beam pattern of a 8-element array showing calibrated beams at -58°, -30°, -0°, 30° and 56° in blue, while the uncalibrated beams are depicted in red.

# 5

# Results

## 5.1 Scan Loss Impact

Assuming an error-free phase shift among the elements of an 8-element array, as in 3.8, Figure 5.1 demonstrates the diminution of gain when the beam is directed at a $\theta_0 = 60°$ angle versus a boresight orientation. Table 5.1 shows the comparative gains for 4- and 8-element arrays at $\theta_0 = 60°$ and $\theta_0 = 0°$, including the peak gain values. The data reveal that employing linear progressive phase shifts yields gain diminishing as the beam diverges from the boresight position. The active element pattern for both antennas is obtained from [21].

Table 5.1: Gain at boresight and $\theta_0 = 60°$ of 4- and 8- element array

| - | 4-element array | 8-element array |
|---|---|---|
| $\text{Gain}_{\theta_0=0°}$ | 26.11 dBi | 32.30 dBi |
| $\text{Gain}_{\theta_0=60°}$ | 20.69 dBi | 26.83 dBi |

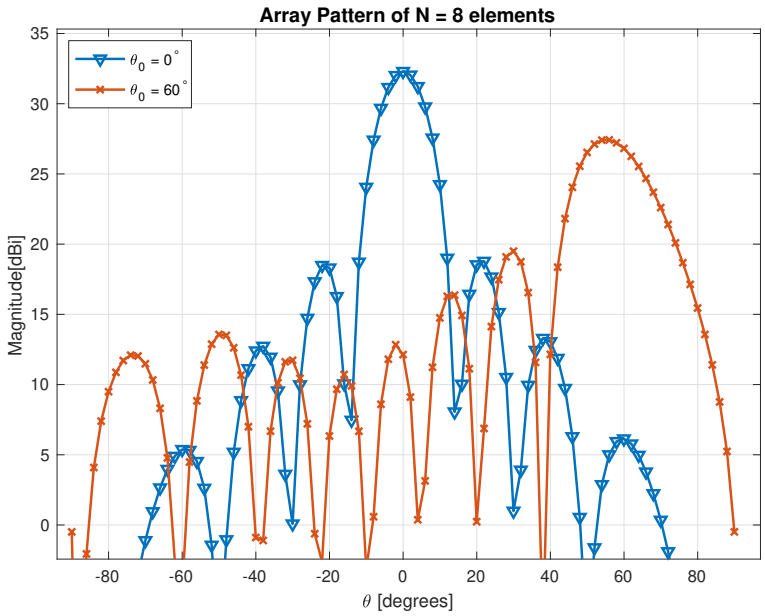


Figure 5.1: Radiation pattern of an 8-element array at boresight and $\theta_0 = 60°$, illustrating scan loss

## 5.2 Study of Phase Shifter Error

Table 5.2 and 5.3 present an example of a 4-element and 8-element linear array designed to steer the beam by 60° away from the boresight direction, utilizing various PSs in accordance with Equation 3.8. It is evident from the table that PSs with a higher number of bits (N-bits) yield more accurate approximations. While higher-bit PSs offer more precise quantized phase shifts, a comparison demonstrates that a 4-bit PS achieves comparable gain to a 9-bit PS in a 4-element array antenna. For an 8-element array only a negligible 0.01 dB difference in gain is achieved which translates to 0.12% range degradation according to 3.12, suggesting that 4-bit PSs are sufficiently effective for beam steering, avoiding the need for more complex and costly alternatives. Figures 5.2 and 5.3 show the beam direction at $\theta_0 = 60°$ for 4-element and 8-element arrays using different PSs, respectively. These Figures demonstrate that as the bit count of PSs decreases, the side lobes become more pronounced and the gain is reduced.

Table 5.2: The values of the progressive linear phase shifts of 4-element array using different PSs at $\theta_0 = 60°$

| - | m = 1 | m = 2 | m = 3 | m = 4 | Gain [dBi] |
|---|---|---|---|---|---|
| $\psi_m$ | 0° | 155.89° | 311.77° | 107.65° | 20.69 |
| 9-bits PS | 0° | 156.09° | 311.48° | 107.58° | 20.69 |
| 4-bits PS | 0° | 157.5° | 315° | 112.5° | 20.69 |
| 3-bits PS | 0° | 135° | 315° | 90° | 20.54 |
| 2-bits PS | 0° | 180° | 270° | 90° | 19.86 |
| 1-bit PS | 0° | 180° | 360° | 180° | 19.74 |

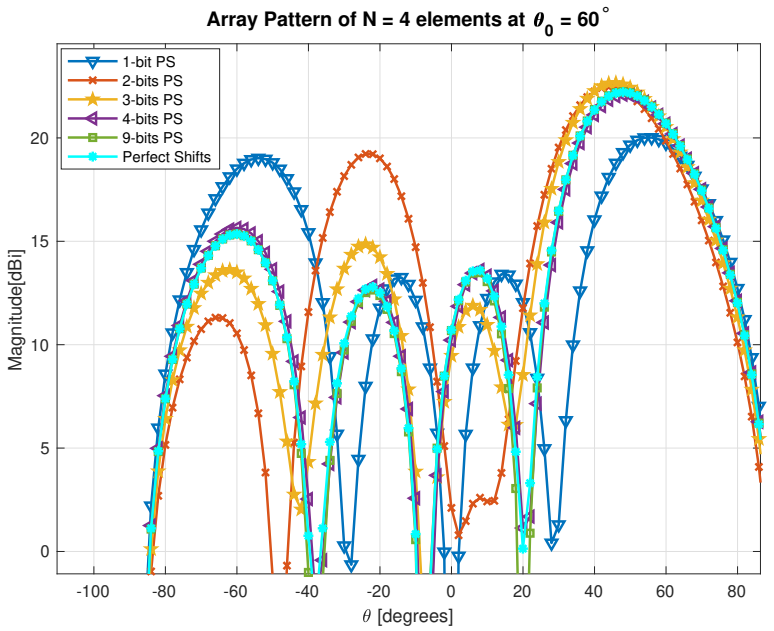


Figure 5.2: Radiation pattern of a 4-element array at $\theta_0 = 60°$ using different PSs, demonstrating that 4-bit and higher PSs produce patterns closely resembling the theoretical model.

Table 5.3: The values of the progressive linear phase shifts of 8-element array using different PSs at $\theta_0 = 60°$

| - | m = 1 | m = 2 | m = 3 | m = 4 | m = 5 | m = 6 | m = 7 | m = 8 | Gain [dBi] |
|---|---|---|---|---|---|---|---|---|---|
| $\psi_m$ | 0° | 155.89° | 311.77° | 107.65° | 263.54° | 59.42° | 215.31° | 11.19° | 26.83 |
| 9-bits PS | 0° | 156.09° | 311.48° | 107.58° | 263.67° | 59.77° | 215.16° | 11.25° | 26.83 |
| 4-bits PS | 0° | 157.5° | 315° | 112.5° | 270° | 67.5° | 225° | 0° | 26.82 |
| 3-bits PS | 0° | 135° | 315° | 90° | 270° | 45° | 225° | 0° | 26.66 |
| 2-bits PS | 0° | 180° | 270° | 90° | 270° | 90° | 180° | 0° | 26.00 |
| 1-bit PS | 0° | 180° | 0° | 180° | 180° | 0° | 180° | 0° | 23.22 |

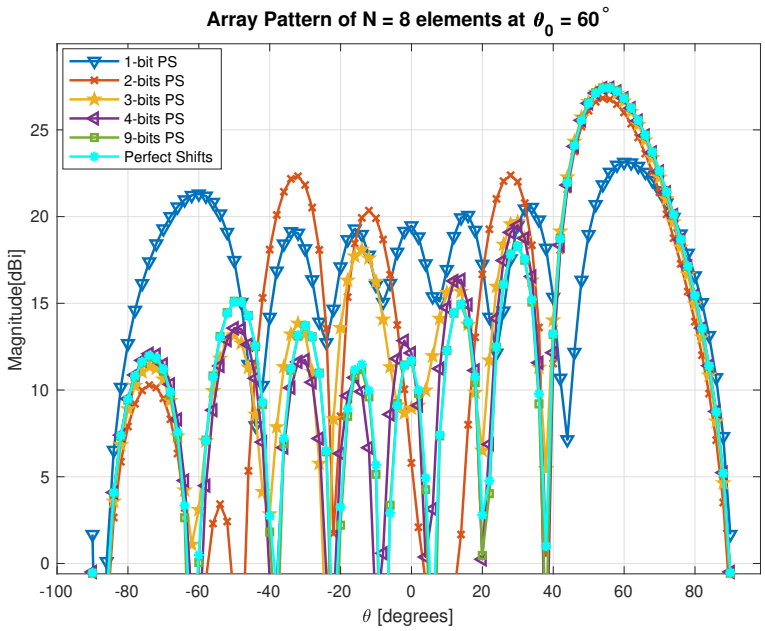


Figure 5.3: Radiation pattern of a 8-element array at $\theta_0 = 60°$ using different PSs, demonstrating that 4-bit and higher PSs produce patterns closely resembling the theoretical model.

## 5.3 Study of Amplitude Perturbation

This section discusses the application of amplitude perturbations to the excitation amplitudes, as outlined in the total electric field equation 3.7, utilizing the attenuator described in 3.5.2. It is premised on achieving perfect phase shifts from 3.8 for beam steering at $\theta_0 = 60°$, with the radiation pattern derived from 3.7. The electric field for a 4-element array is obtained following the methodology in [21]. The study examines two perturbation types: random and systematic amplitude perturbations. Various ranges of amplitude perturbation are analyzed to demonstrate the associated performance degradation.

Random perturbation refers to each array element experiencing a random amplitude excitation error within ± amplitude perturbation. Conversely, systematic perturbation involves each array element's amplitude deviating by a constant value, $P_{step}$, from its adjacent element. Both perturbation types ensure the sum of squared amplitudes in linear terms equals four for a 4-element array and 8 for an 8-element array.

Figure 5.4 illustrates the variance in gain compared to an unperturbed scenario over 1000 iterations with an amplitude perturbation of ±1 dB. It reveals the maximum gain reductions recorded at 20.48 dBi for the 4-element array and 25.90 dBi for the 8-element array. The average gains were 20.64 dBi and 26.53 dBi for the 4- and 8-element arrays respectively. Plugging these values, which represent the largest deviations, into 3.12 indicates a range reduction of 2.39% for the 4-element array and 10% for the 8-element array. Over 1000 iterations on a 16-element array

with the same amplitude perturbation and given that the theoretical value is 32.92 dBi, the minimum gain obtained was 32.57 dBi and the average gain was 32.78 dBi. This corresponds to a range loss of 4% and 1%, respectively. Table 5.4 presents the average and minimum gains associated with various amplitude perturbations, along with the resulting range reductions for both 4- and 8-element arrays.

Table 5.4: The average/minimum gains and the corresponding range reduction at $\theta = 60°$ for different random amplitude perturbation for 4- and 8-element array over 1000 iterations

| - | $\text{Gain}_{4-element}$ [dBi] | Range Loss | $\text{Gain}_{8-element}$ [dBi] | Range Loss |
|---|---|---|---|---|
| No perturbation | 20.69 | 0/0 % | 26.82 | 0/0 % |
| ±0.5 dB | 20.68/20.62 | 0.18/0.76 % | 26.78/26.64 | 0.49/2 % |
| ±0.7 dB | 20.67/20.58 | 0.28/1.3 % | 26.75/26.51 | 0.8/3.5 % |
| ±1 dB | 20.64/20.50 | 0.5/2.39 % | 26.70/26.37 | 1.4/5.1 % |
| ±1.2 dB | 20.63/20.44 | 0.71/2.8 % | 26.65/26.27 | 1.91/6.17 % |
| ±1.5 dB | 20.60/20.23 | 1/5.1 % | 26.60/26.10 | 2.56/7.94 % |

Additionally, systematic amplitude perturbations ranging from $P_{step} = 0.1$ dB to $P_{step} = 1.6$ dB were analyzed to understand their effect on the radiation pattern, shown in Figure 5.5 and 5.6. Clearly, increasing $P_{step}$ leads to higher side lobe levels and a more significant gain reduction at $\theta = 60°$. Table 5.5 illustrates the gain reduction at $\theta_0 = 60°$ for all $P_{step}$ values and the corresponding range reduction for 4- and 8-element arrays.

The results indicate that systematic amplitude perturbation significantly affects antenna performance more adversely than random perturbation, leading to greater performance degradation. An analysis of both types of amplitude perturbations demonstrates that antennas with a higher number of array elements are particularly sensitive to such perturbations. For example, with a step size of $P_{step} = 1.5$ dB, the 8-element array experiences a range loss of 20%, which is substantially higher than the loss observed in the 4-element array which is 7.04%. Similarly, the range loss due to random amplitude perturbation is more pronounced in the 8-element array, where it reaches 7.94% for the minimum obtained gain and a perturbation of ±1.5 dB. In contrast, the 4-element array experiences a smaller range loss of 5.1%.

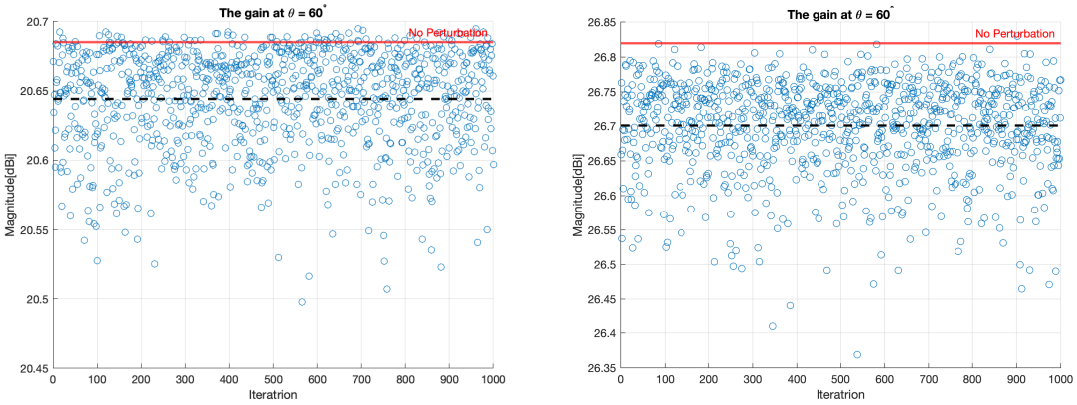


(a) 4-element array (b) 8-element array

Figure 5.4: Gains at $\theta = 60°$ across 1000 iterations with $\pm 1$ dB amplitude perturbation, where the red line represents the theoretical gain and the dashed black line indicates the average gain.

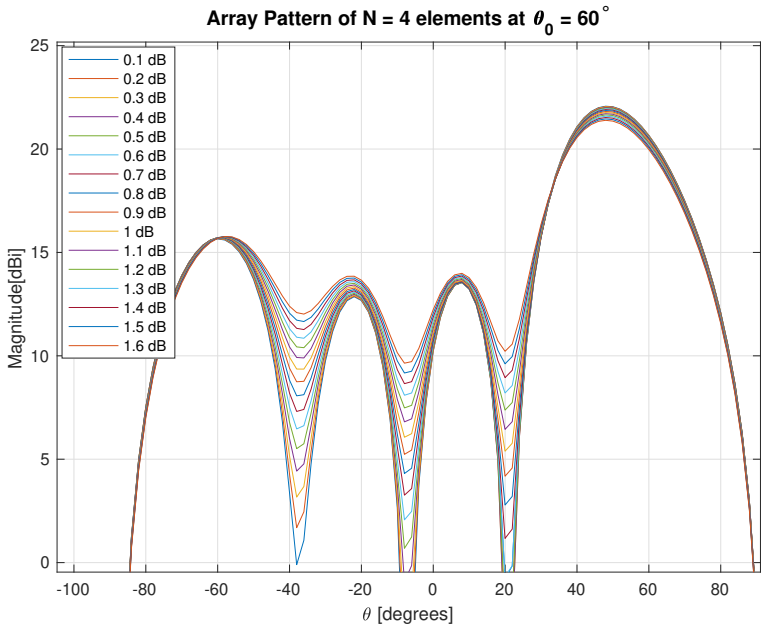


Figure 5.5: Impact of systematic amplitude perturbations on the radiation pattern at $\theta_0 = 60°$ for a 4-element array, with $P_{step}$ ranging from 0.1 dB to 1.6 dB.

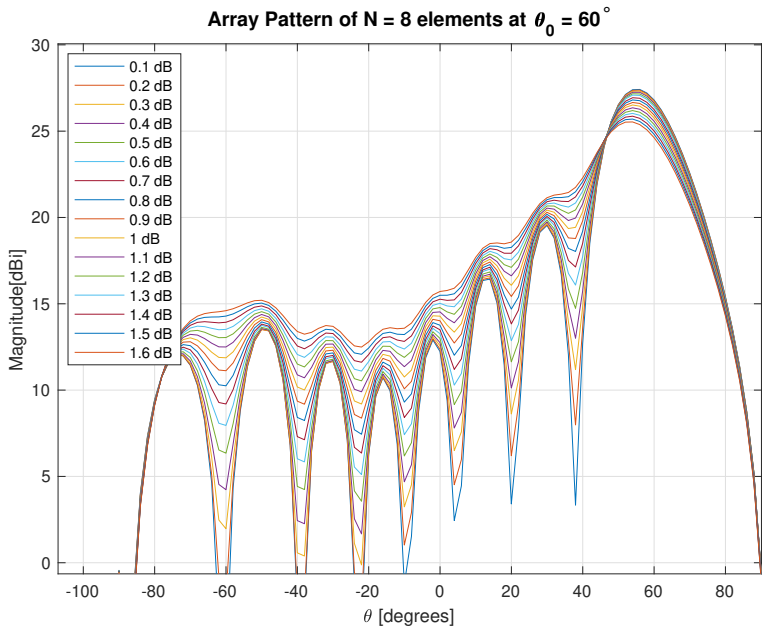


Figure 5.6: Impact of systematic amplitude perturbations on the radiation pattern at $\theta_0 = 60°$ for a 8-element array, with $P_{step}$ ranging from 0.1 dB to 1.6 dB.

Table 5.5: The gains and the corresponding range reduction at $\theta = 60°$ for different systematic amplitude perturbation for 4- and 8-element array

| $P_{step}$ | $\text{Gain}_{4-element}$ [dBi] | Range Loss | $\text{Gain}_{8-element}$ [dBi] | Range Loss |
|---|---|---|---|---|
| 0 dB | 20.69 | 0% | 26.82 | 0% |
| ±0.1 dB | 20.67 | 0.22% | 26.81 | 0.11% |
| ±0.2 dB | 20.66 | 0.33% | 26.76 | 0.64% |
| ±0.3 dB | 20.65 | 0.51% | 26.70 | 1.40% |
| ±0.4 dB | 20.62 | 0.76% | 26.63 | 2.19% |
| ±0.5 dB | 20.60 | 1.07% | 26.53 | 3.34% |
| ±0.6 dB | 20.56 | 1.44% | 26.43 | 4.38% |
| ±0.7 dB | 20.53 | 1.87% | 26.26 | 6.26% |
| ±0.8 dB | 20.48 | 2.36% | 26.11 | 7.88% |
| ±0.9 dB | 20.43 | 2.9% | 25.94 | 9.66% |
| ±1 dB | 20.38 | 3.5% | 25.77 | 11.40% |
| ±1.1 dB | 20.32 | 4.13% | 25.58 | 13.31% |
| ±1.2 dB | 20.26 | 4.81% | 25.39 | 15.14% |
| ±1.3 dB | 20.20 | 5.52% | 25.21 | 16.96% |
| ±1.4 dB | 20.13 | 6.26% | 25.02 | 18.75% |
| ±1.5 dB | 20.06 | 7.04% | 24.83 | 20.53% |
| ±1.6 dB | 19.98 | 7.84% | 24.63 | 22.27% |

## 5.4 Mechanical Error Impact on Radiation Pattern

To examine performance effects under mechanical distortion, we incorporate specific distortion factors into the N-linear array's electric field, based on scenarios in 3.9.3. Beginning with $\theta_0 = 0°$, it is observed that an increase in distortion, measured in terms of $\lambda$, leads to a deterioration in the radiation pattern characterized by reduced gain and elevated side lobe levels. This degradation results from the destructive interference in the far field between the array elements' radiation. Figure 5.7 illustrates these effects through the examination of bent slab distortions applied to a 4-element array. A similar pattern of degradation is observed for an 8-element array, as shown in Figure 5.8. Notably, when $z_{max}$ exceeds $0.5\lambda$ up to $\lambda$, the elements of the 4-array begin to exhibit constructive interference, as demonstrated in Figure 5.9. With an increase in the number of elements within the array antenna, the interference arising from mechanical distortion becomes a complex mixture of constructive and destructive interactions. This leads to a notable degradation in performance correlated with $z_{max}$, as demonstrated for an 8-element array in Figure 5.10. The analysis clearly demonstrates a direct relationship between displacement and performance degradation.

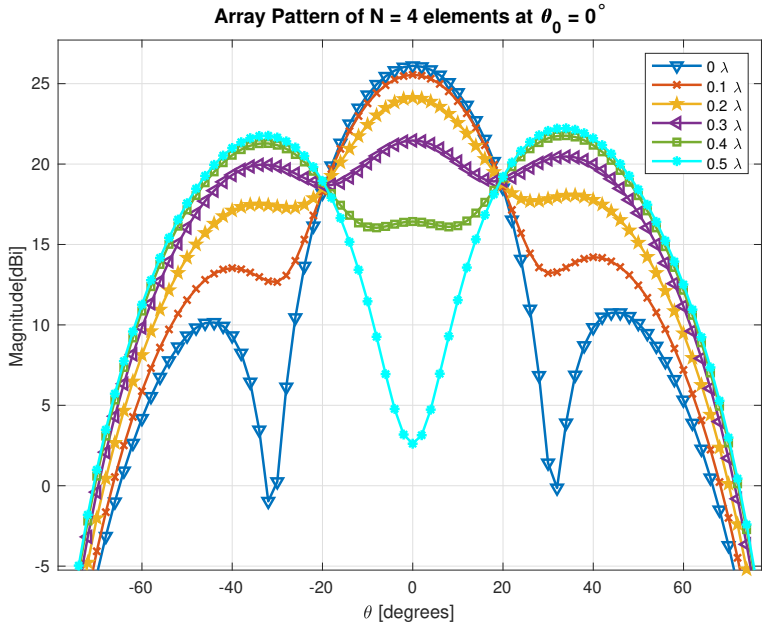


Figure 5.7: Radiation pattern of a 4-element array at $\theta_0 = 0$ influenced by bent slab distortion, with $z_{max}$ ranging from $0\lambda$ to $0.5\lambda$.

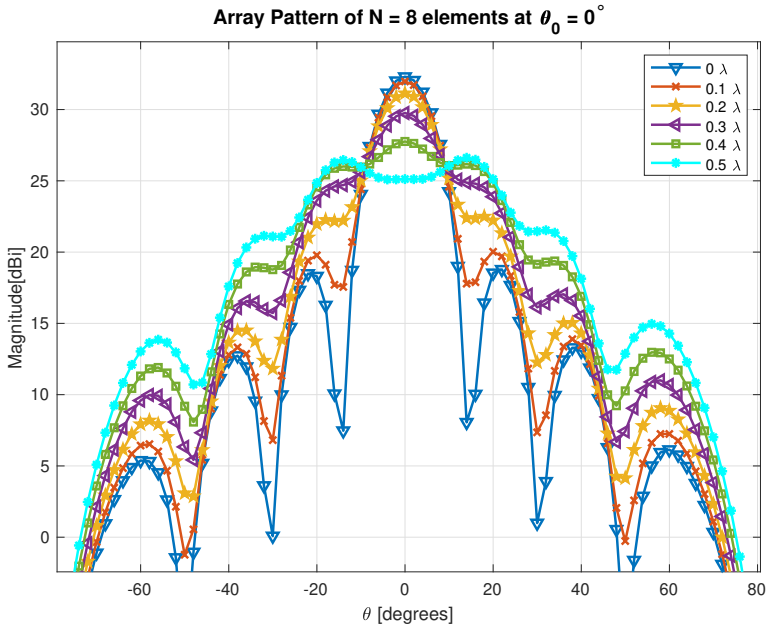


Figure 5.8: Radiation pattern of a 8-element array at $\theta_0 = 0$ influenced by bent slab distortion, with $z_{max}$ ranging from $0\lambda$ to $0.5\lambda$.

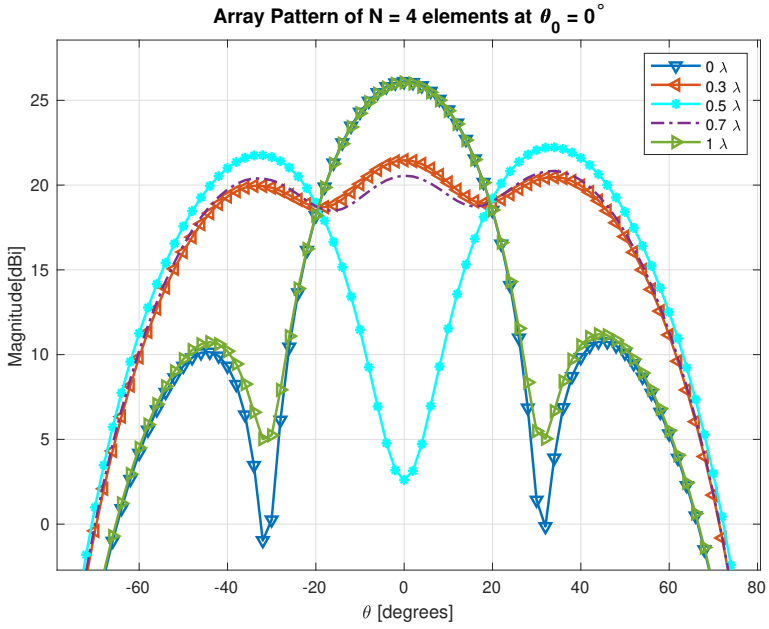


Figure 5.9: Radiation pattern of a 4-element array at $\theta_0 = 0$ due to bent slab distortion, showing constructive interference with $z_{max}$ ranging from $0.5\lambda$ up to $1\lambda$.

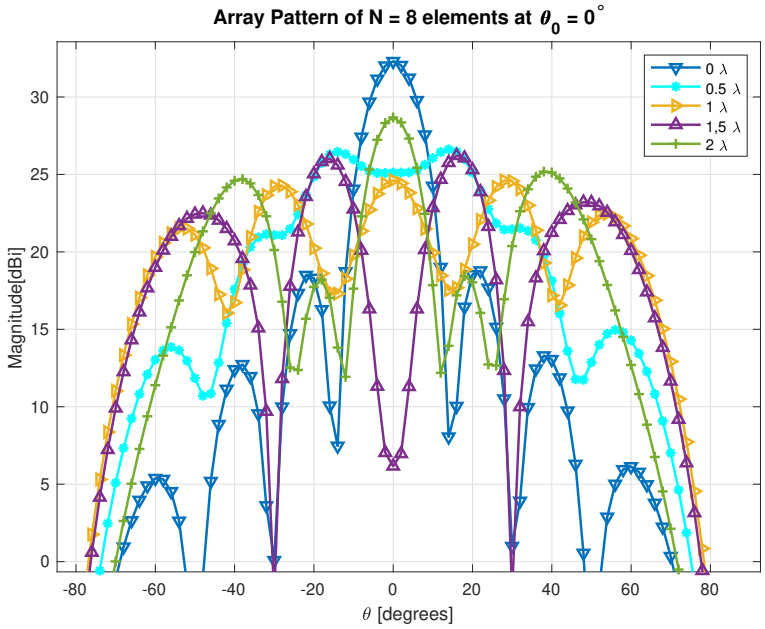


Figure 5.10: Radiation pattern due to bent slab distortion of the 8-element array at $\theta_0 = 0$, showing constructive interference with $z_{max}$ ranging from $0.5\lambda$ up to $2\lambda$.

### 5.4.1 Phase Shifter Precision in Deterministic Error Calibration

As outlined in 3.4.2, the minimum phase shift achievable by an N-bit PS is $\frac{360°}{2^N}$. This limitation means that phase errors smaller than this minimum shift cannot be corrected. To explore the significance of PS precision, let's assume that deterministic mechanical errors can be analytically determined. Thus, the signal from each element would need to be adjusted according to 3.24 to correct for these mechanical discrepancies. Assuming $z_{max} = 0.5\lambda$ and the beam is steered at $\theta_0 = 60°$, various N-bit PSs are utilized to offset the mechanical distortions, and the resultant radiation patterns for both 4 and 8-element arrays are depicted in Figures 5.11 and 5.12. The gain measurements at $\theta = 60°$, listed in Table 5.6, demonstrate that PSs with more than 4-bits are unnecessary, as 4-bits are adequate for compensating the deterministic errors. Figures 5.13 and 5.14 show the radiation pattern after calibration using 4-bit PSs in comparison to a distortion-free scenario, where the only observable difference is a minor deviation in side lobe levels, deemed negligible.

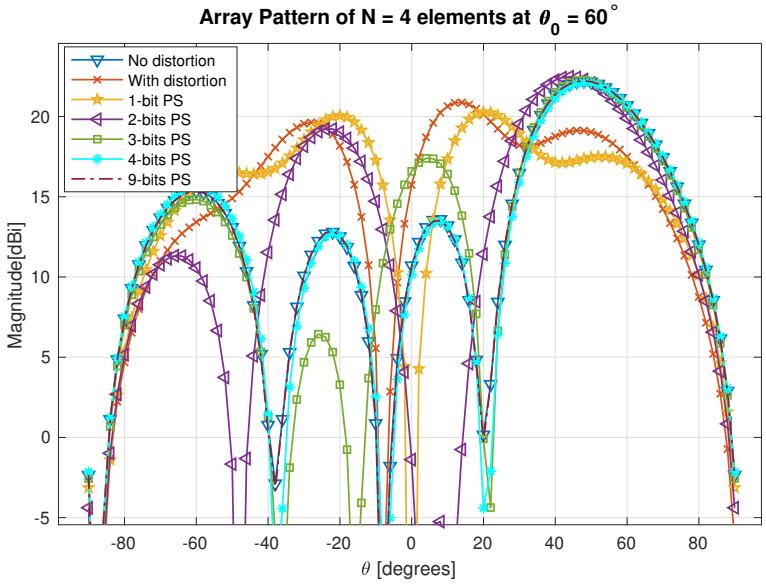


Figure 5.11: Radiation pattern of 4-element array after compensating for the bent slab mechanical error when $z_{max} = 0.5\lambda$ using different PSs when $\theta_0 = 60°$, demonstrating that 4-bit and higher PSs produce patterns closely resembling the theoretical model.

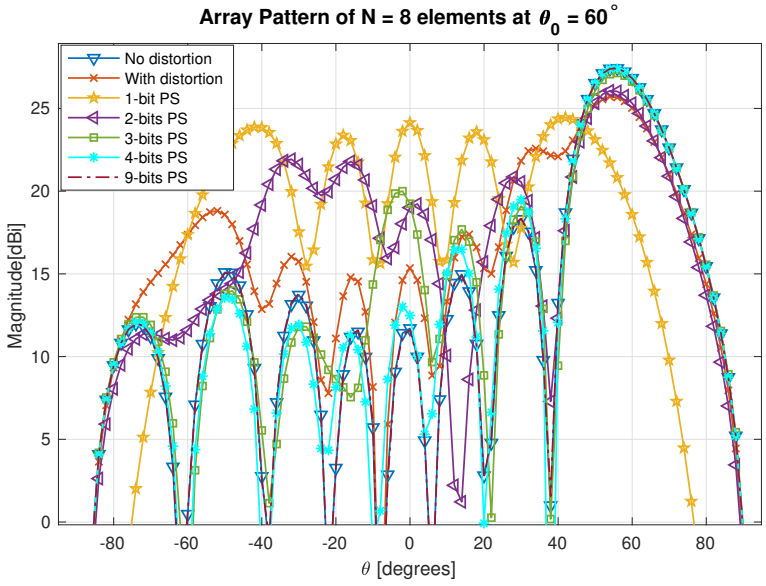


Figure 5.12: Radiation pattern of 8-element array after compensating for the bent slab mechanical error when $z_{max} = 1.5\lambda$ using different PSs when $\theta_0 = 60°$, demonstrating that 4-bit and higher PSs produce patterns closely resembling the theoretical model.

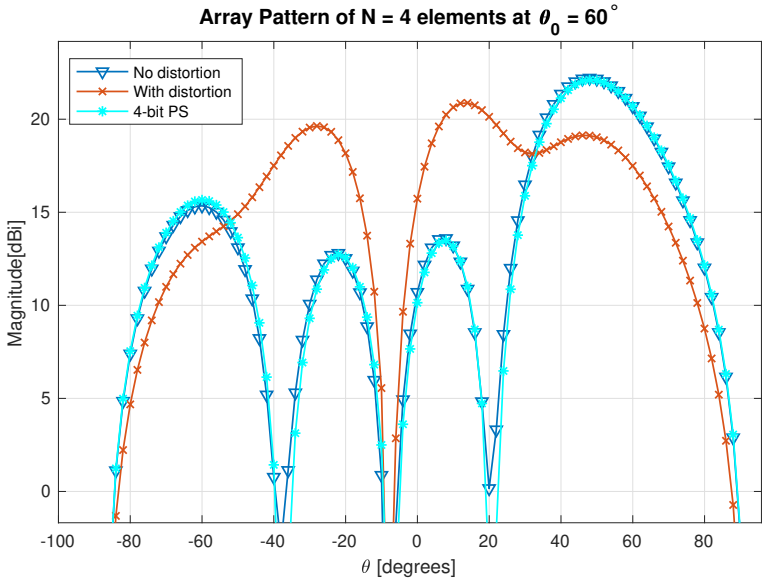


Figure 5.13: Radiation pattern of 4-element array after compensating for the bent slab mechanical error when $z_{max} = 0.5\lambda$ using 4-bit PSs when $\theta_0 = 60°$.

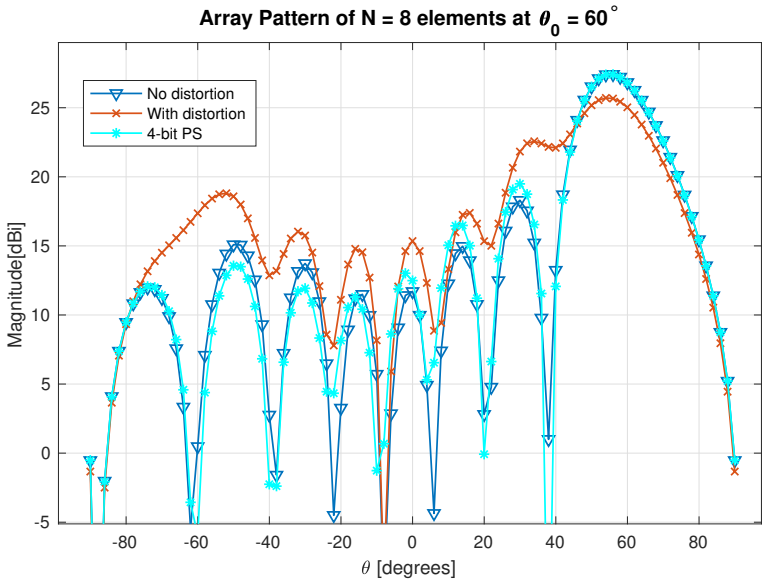


Figure 5.14: Radiation pattern of 8-element array after compensating for the bent slab mechanical error when $z_{max} = 1.5\lambda$ using 4-bit PSs when $\theta_0 = 60°$.

Table 5.6: The obtained gains using different PSs to compensate for mechanical errors when $\theta_0 = 60°$

| - | Bent Slab | |
|---|---|---|
| - | $\text{Gain}_{4element}$ [dBi] | $\text{Gain}_{8element}$ [dBi] |
| Without distortion | 20.69 | 26.83 |
| With distortion | 17.49 | 25.40 |
| 9-bits PS | 20.69 | 26.83 |
| 4-bits PS | 20.70 | 26.82 |
| 3-bits PS | 20.56 | 26.62 |
| 2-bits PS | 19.89 | 25.32 |
| 1-bit PS | 17.07 | 18.60 |

## 5.5 Mismatch Loss Uncertainties in TX/RX Modules

To demonstrate the effects of component mismatches, this study calculates the phase and amplitude variations across the transmitter (TX) and receiver (RX) chains, using equations 3.19 and3.20, under the assumption that both the transmitter and receiver substrates have a permittivity of $\epsilon = 2.2$, as noted in [59]. Given that this work primarily targets components operating at a frequency of 100 GHz with a bandwidth of 10 GHz, it is presumed that the components selected are optimized for the specified frequency range, exhibiting comparable performance characteristics. The components chosen for this analysis are originally designed to function at frequencies around or above 100 GHz, validating the assumptions made regarding their applicability and performance at the desired operational frequency.

Components are specifically designed to minimize signal reflection at their target frequency, making it crucial to examine the effects of mismatches at the bandwidth's boundaries, where increased signal reflection can significantly impair performance. Moreover, as a phased array antenna's beam angles away from the direct forward position, it encounters greater signal reflection. Thus, the scenarios that likely represent the most significant mismatch losses occur at frequencies of 95 and 105 GHz, especially when the beam's steering angle, $\theta_0$, is $\pm 60°$. The overall deviations in amplitude and phase due to these mismatches represent the cumulative effects of component losses within the transmitter (TX) and receiver (RX) chains. Detailed in Table 5.7 are the specific amplitude and phase deviations for both transmission and reception modules at the specified edge frequencies of 95 and 105 GHz.

Table 5.7: The amplitude/phase deviations ($\Delta_{amplitude}$ [dB]/$\Delta_{phase}$ [°]) at 95 and 105 GHz for TX and RX chains when $\theta_0 = 60°$.

| - | Antenna - PB | PB - LNA/PA | LNA/PA - PS | PS - Attenuator | total |
|---|---|---|---|---|---|
| $TX_{f=95}$ | ± 0.19/1.28° | ± 0.12/0.80° | ± 0.24/1.64° | ± 0.53/3.16° | ± 1.09/7.32° |
| $RX_{f=95}$ | ± 0.06/0.41° | ± 0.27/1.81° | ± 0.38/2.56° | ± 0.24/1.61° | ± 0.95/6.39° |
| $TX_{f=105}$ | ± 0.12/0.81° | ± 0.11/0.72° | ± 0.24/1.64° | ± 0.15/1.02° | ± 0.63/4.16° |
| $RX_{f=105}$ | ± 0.04/0.26° | ± 0.34/2.28° | ± 0.27/1.81° | ± 0.12/0.81° | ± 0.77/5.16° |

The impact of mismatch losses in the transmitter and receiver chains is minimal. To highlight the consequences of these losses on the antenna's radiation pattern, we examine the most challenging situation, which occurs in the transmitter chain at 95 GHz. The radiation pattern generated under this scenario, depicted in figures 5.15 and 5.16, reflects amplitude and phase deviations over 1000 iterations, providing insight into the pattern's variability due to mismatch losses. Analysis of the gain at $\theta = 60°$ across 1000 iterations reveals that mismatch losses minimally affect performance, with a maximum gain reduction of 0.26 dBi for a 4-element array and 0.49 dBi for an 8-element array. Consequently, based on the range equation 3.12, the operational range decreases by only 2.8% for the 4-element array and 5.5% for the 8-element array. After examining the mismatch loss at the transmitter chain of a 16-element array at 95 GHz across 1000 iterations, the findings revealed that the average gain achieved was 32.75 dBi, with an associated range loss of 2%. The lowest observed gain was 32.43 dBi, resulting in a range loss of 5%, while the maximum gain at $\theta = 60°$ was 32.9 dBi. These results indicate that the 16-element array is less affected by mismatch loss compared to the 8-element array.

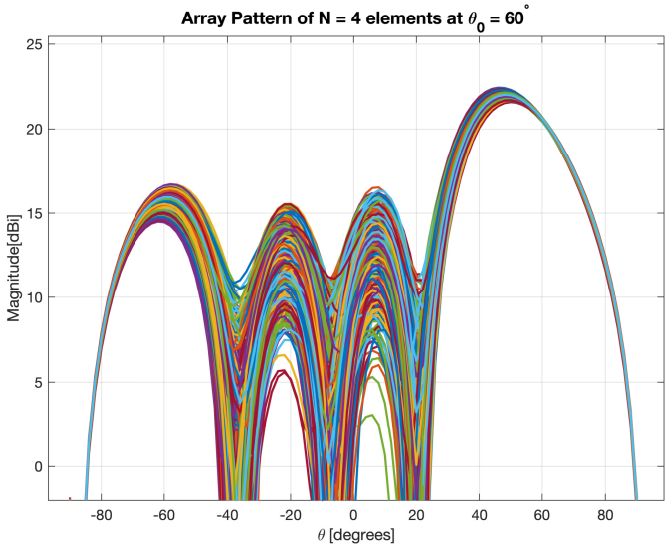


Figure 5.15: Radiation pattern of the 4-element array having random amplitude of ±1.09 dB and phase perturbation of ±7.32° due to mismatch losses at $\theta_0 = 60°$ in TX chain at 95 GHz.

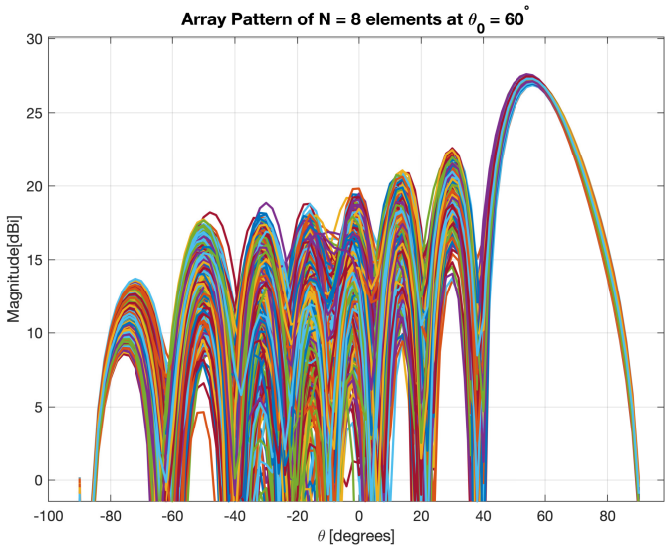


Figure 5.16: Radiation pattern of the 8-element array having random amplitude of $\pm 1.09$ dB and phase perturbation of $\pm 7.32°$ due to mismatch losses at $\theta_0 = 60°$ in TX chain at 95 GHz.

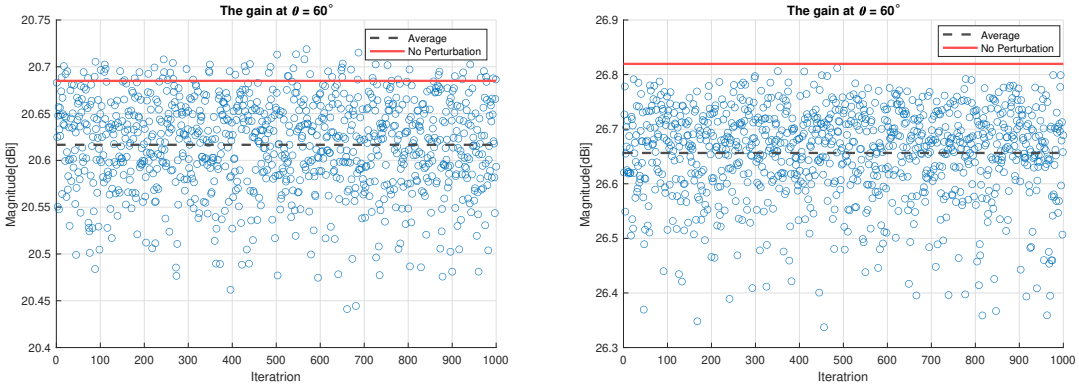


(a) 4-element array

(b) 8-element array

Figure 5.17: Gains at $\theta = 60°$ across 1000 iterations at 95 GHz, where the red line represents the theoretical gain and the dashed black line indicates the average gain.

## 5.6 Temperature Impact on Radiation Pattern

In many applications, it's crucial to assess the antenna's tolerance to temperature fluctuations and implement necessary calibrations to maintain performance across varying conditions. Therefore, the effects of temperature variations ranging from -45°C to 85°C are examined. The maximum phase error due to temperature change based on 3.26 is 4.3°C which has negligible impact on the performance. Instead, the additional phase shifts caused by thermal drift, calculated here as 0.6°/ °C is studied. For instance, at 85°C, the cumulative phase shift is $(85 - T_{ref}) \times 0.6 = 39$ degrees, where $T_{ref}$ is the reference temperature which is assumed 20°C. If all array

elements undergo the same phase shift, the radiation pattern remains unchanged. However, in reality, the phase shifts are not uniform across the phased array elements. Instead, for each channel the phase shifts in this work are modeled as having a random value of $\pm p \times T \times 0.6$, where $T$ is the temperature and $p$ represents a percentage deviation, to demonstrate how phase variations due to thermal drift can degrade performance.

Starting from a high temperature of 85°C with $p = 50\%$ and an initial angle $\theta_0 = 60°$, over 1000 iterations, the observed gains at $\theta = 60°$ for 4-element array are presented in Figure 5.18. The average gain reduction is 0.14 dBi compared to the unperturbed case, while the most significant reduction observed is 0.55 dBi. According to the referenced data, this translates to a 6% decrease in range. Table 5.8 displays the gains obtained for several values of $p$ for 4- and 8-element array. Clearly, as the deviation in phase distribution increases worse gains are achieved indicating the necessity for calibration. It has been observed that the gain drops less for the 8-element array than for the 4-element indicating that increasing the number of array elements leads to less sensitivity to phase deviations. Based on the data from Table 5.8 and according to 3.12, the range experiences a reduction of more than 6% when $p$ exceeds 50% for the 4-element array. This underscores the necessity of implementing calibration across various temperatures to mitigate the effects of temperature on performance. Assuming a phase deviation of 50%, i.e., $p = 50\%$, the resulting gains at temperatures within the targeted range of [-45°C, 85°C] are documented in Table 5.9. This table presents the outcomes for 4- and 8-element array antennas across 1000 iterations. The required temperatures for calibration depend on the acceptable level of gain reduction. If a range loss exceeding 6% is not permissible, calibration is necessary, as demonstrated at a temperature of 85°C for the 4-element array.

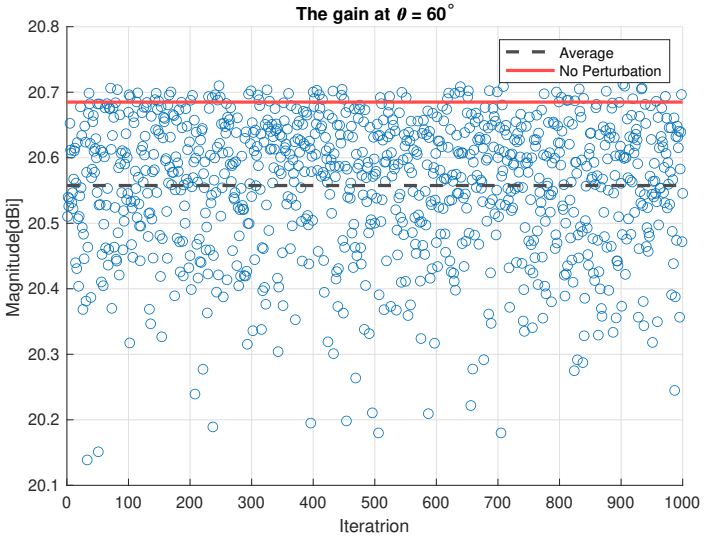


Figure 5.18: The obtained gains of 1000 iteration due to thermal shift at T = 85°C and $p = 50\%$ of 4-element array, where the red line represents the theoretical gain and the dashed black line indicates the average gain.

Table 5.8: The average/minimum gains at $\theta = 60°$ and T = 85°C with different $p$ for 4- and 8-element array over 1000 iterations

| - | $\text{Gain}_{4-element}$ [dBi] | Range Loss | $\text{Gain}_{8-element}$ [dBi] | Range Loss |
|---|---|---|---|---|
| No perturbation | 20.69 | - | 26.82 | - |
| $p = 10\%$ | 20.68/20.63 | 0.1%/0.7% | 26.81/26.79 | 0.1%/0.34% |
| $p = 20\%$ | 20.67/20.57 | 0.2%/1% | 26.80/26.73 | 0.2%/1% |
| $p = 30\%$ | 20.64/20.44 | 0.6%/3% | 26.76/26.63 | 0.7%/2% |
| $p = 40\%$ | 20.60/20.27 | 1%/5% | 26.73/26.56 | 1%/3% |
| $p = 50\%$ | 20.56/20.14 | 2%/6% | 26.67/26.42 | 2%/5% |

Table 5.9: The average/minimum gains at $\theta = 60°$ at different T with $p = 50\%$ for 4- and 8-element array over 1000 iterations

| - | $\text{Gain}_{4-element}$ [dBi] | Range Loss | $\text{Gain}_{8-element}$ [dBi] | Range Loss |
|---|---|---|---|---|
| T = -45°C | 20.56/20.10 | 2%/7% | 26.68/26.46 | 2%/4% |
| T = -35°C | 20.59/20.27 | 1%/5% | 26.71/26.55 | 1%/3% |
| T = -25°C | 20.63/20.36 | 0.7%/4% | 26.75/26.62 | 0.8%/2% |
| T = -15°C | 20.65/20.48 | 0.5%/3% | 26.78/26.70 | 0.5%/1% |
| T = -5°C | 20.67/20.55 | 0.2%/2% | 26.80/26.74 | 0.2%/1% |
| T = 5°C | 20.67/20.63 | 0.2%/1% | 26.81/26.78 | 0.1%/0.5% |
| T = 15°C | 20.69/20.67 | 0%/0.2% | 26.82/26.81 | 0%/0.1% |
| T = 25°C | 20.69/20.67 | 0%/0.2% | 26.82/26.81 | 0%/0.1% |
| T = 35°C | 20.68/20.62 | 0.1%/1% | 26.81/26.78 | 0.1%/0.5% |
| T = 45°C | 20.67/20.55 | 0.2%/2% | 26.80/26.74 | 0.2%/1% |
| T = 55°C | 20.65/20.49 | 0.5%/3% | 26.78/26.68 | 0.5%/2% |
| T = 65°C | 20.63/20.38 | 0.7%/4% | 26.75/26.62 | 0.7%/3% |
| T = 75°C | 20.59/20.25 | 1%/5% | 26.72/26.52 | 1%/4% |
| T = 85°C | 20.56/20.14 | 2%/6% | 26.67/26.42 | 2%/5% |

The radiation patterns for 4-element and 8-element arrays at the boresight, where amplitudes are compromised due to temperature variations, are depicted in figures 5.19 and 5.20, respectively. The corresponding gains and range losses at different temperatures are presented in table 5.10. It is evident that within a temperature range of -5 to 55 degrees Celsius, the impact of temperature on performance is minimal, where the range loss remains below 5%. Outside this temperature range, calibration becomes necessary when range losses exceed 6%.

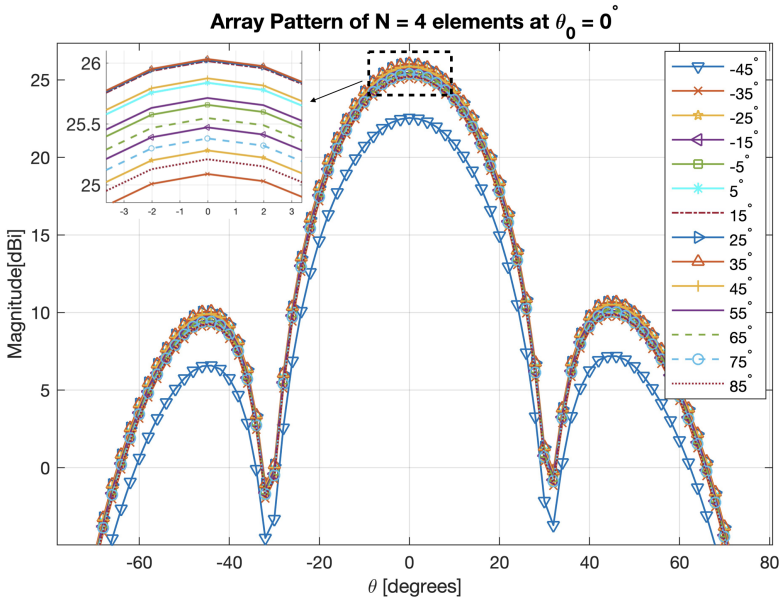


Figure 5.19: Impact of temperature variations from -45°C to 85°C on the radiation pattern at boresight of a 4-element array, highlighting the amplitude error-induced degradation, with the most severe impact observed at -45°C.

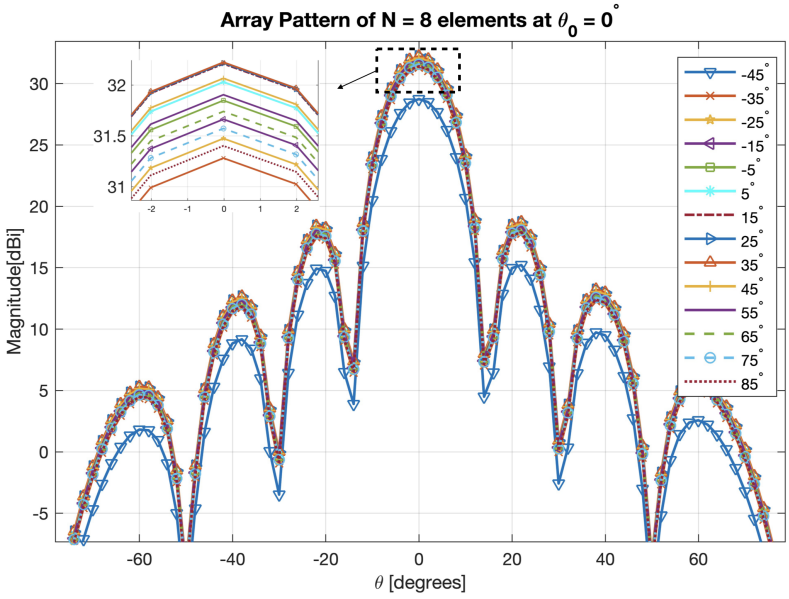


Figure 5.20: Impact of temperature variations from -45°C to 85°C on the radiation pattern at boresight of a 8-element array, highlighting the amplitude error-induced degradation, with the most severe impact observed at -45°C.

Table 5.10: The gains at boresight at different T affecting the amplitudes for 4- and 8-element.

| - | $Gain_{4-element}$ [dBi] | Range Loss | $Gain_{8-element}$ [dBi] | Range Loss |
|---|---|---|---|---|
| T = -45°C | 22.55 | 34% | 28.74 | 34% |
| T = -35°C | 25.09 | 11% | 31.28 | 11% |
| T = -25°C | 25.28 | 9% | 31.47 | 9% |
| T = -15°C | 25.47 | 7% | 31.66 | 7% |
| T = -5°C | 25.66 | 5% | 31.85 | 5% |
| T = 5°C | 25.84 | 3% | 32.03 | 3% |
| T = 15°C | 26.01 | 1% | 32.21 | 1% |
| T = 25°C | 26.03 | 1% | 32.22 | 1% |
| T = 35°C | 26.03 | 1% | 32.22 | 1% |
| T = 45°C | 25.88 | 3% | 32.07 | 3% |
| T = 55°C | 25.71 | 5% | 31.91 | 5% |
| T = 65°C | 25.55 | 6% | 31.74 | 6% |
| T = 75°C | 25.38 | 8% | 31.57 | 8% |
| T = 85°C | 25.21 | 10% | 31.40 | 10% |

The investigation of thermal expansion effects is performed when the main beam is directed away from the broadside, at angles of $\theta_0 = 60°$. This approach is used to demonstrate the most significant impact of thermal expansion on the antenna's performance. Using the thermal expansion coefficient for an aluminum phased array as in [47] ($\alpha = 2.35 \cdot 10^{-}5\ m/m.k$ ), and applying this value in 3.27 at temperatures of 85°C and -45°C, the expansion in element spacing proves to be negligible. The resulting radiation pattern of the 4-element array is depicted in Figure 5.21, where no noticeable difference in performance is observed and the gain is reduced by 0.001 dBi. On the other side, Figure 5.22 shows the radiation pattern of the 8-element array where a slight difference in side lobe levels is observed. At extreme temperatures, the gain of the 8-element array decreases by just 0.005 dBi, and this reduction becomes even smaller when the temperature is within the central range of the desired interval, leading to a negligible effect on antenna performance. Similar results are obtained at -45°C.

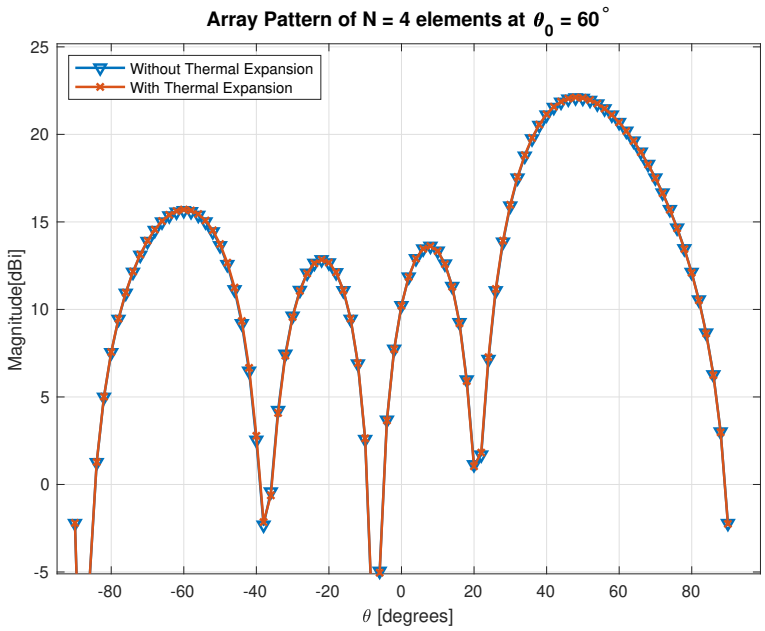


Figure 5.21: Radiation pattern of the 4-element array due to thermal expansion at 85°C, showing that it remains identical to the unaltered pattern at the steering angle.

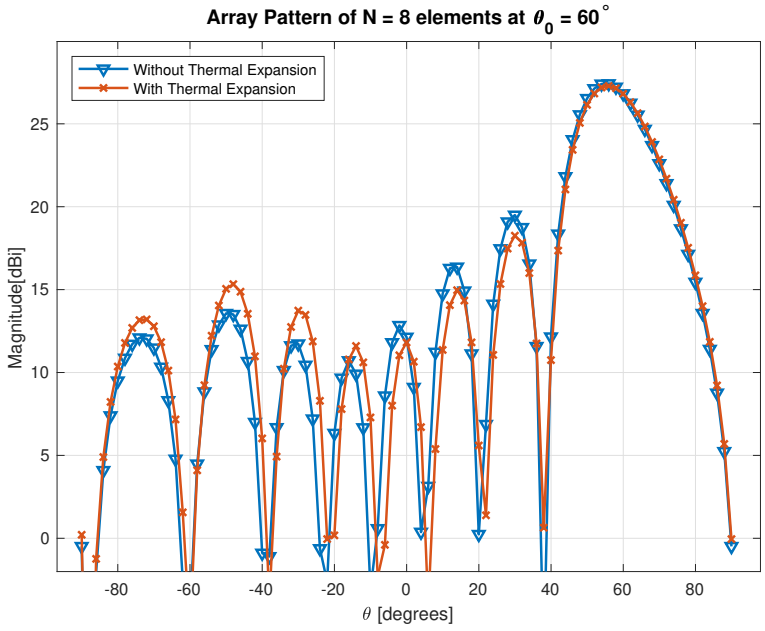


Figure 5.22: Radiation pattern of the 8-element array at 85°C due to thermal expansion, demonstrating a pattern very close to the unaltered radiation pattern at the steering angle.

## 5.7 Calibration Result Analysis

In this section, we use the ON/OFF and mREV methods to calibrate systematic phase errors in the absence of random perturbations. This allows us to evaluate the performance of various calibration algorithms. Given that antenna deformations during manufacturing often exceed simple symmetric distortions such as those seen in bent slabs and bowls, our goal is to calibrate for phase errors arising from both symmetric distortion (bent slab) and irregular phase errors. For bent slab distortion, $z_{max}$ is set at $0.5\lambda$ for a 4-element array and $1.5\lambda$ for an 8-element array, as these values significantly influence the radiation pattern, as illustrated in 5.4. The effectiveness of the algorithms employed does not vary depending on whether the antenna functions in receiving or transmitting chains. As demonstrated previously 5.4.1, a 4-bit PS is sufficiently accurate for use in the calibration process employed here. The calibration is applied to the beams outlined in the beam book for each antenna, as shown in 4.3.

The effectiveness of the calibration can be assessed either by the gains obtained or by the sidelobe levels, depending on the application of the calibrated antenna and which aspect is most critical. In this project, the calibration's success is measured by the radiated power of the main calibrated beams in the beam book. Since the calibration methods involve measuring the radiated power at specific angles listed in the beam book, benchmarks for the calibrated beams must be established to determine if the calibration is satisfactory. Specifically, if the radiated power post-calibration falls below a certain value compared to theoretical expectations, this could indicate that the beams have shifted or that there are higher sidelobe levels, resulting in gains below the predefined threshold. For this project, a calibrated beam that is less than 0.1 dBi below the theoretical value is considered unsuccessful.

### 5.7.1 ON/OFF Calibration Results

Calibrating an M-element linear array using n-bit PS by ON/OFF methods begins by deactivating M-2 elements and adjusting the phases of the first two elements through $(2^n)$ phase states until maximum radiated power is achieved. Subsequently, elements are sequentially activated and tuned for maximum power until all are calibrated. This approach requires $M \times (2^n)$ runs to calibrate phase errors. The gains achieved after calibrating a 4-element and 8-element array, which incorporate bent slab distortion and irregular phase errors, are listed in tables 5.11 and 5.12, respectively, alongside the theoretical gains. Three scenarios of irregular phase errors are examined, with errors randomly varying within $\pm 6$ radians. The results show that the calibrated gains are within 0.1 dBi of theoretical values in all scenarios, indicating successful calibration across various error types and element counts.

Figure 5.23 displays the calibrated beam book for the 4-element array, comparing it with beam books with and without $0.5\lambda$ bent slab distortion. Figure 5.25 shows the beam book for the 4-element array calibrated against irregular phase errors, with corresponding gains noted in table 5.11 as $\text{gain}_{irr3}$. The deviations from

the ideal beam book are minor, and the calibrated results consistently exceed the set threshold.

Similarly, for the 8-element array, the ON/OFF method effectively calibrates both $1.5\lambda$ bent slab distortion and irregular phase errors, as demonstrated in figures 5.24 and 5.26. The gains for the calibrated beams, shown in figure 5.26, are recorded in table 5.12 as $\text{gain}_{irr3}$. As long as the gains post-calibration remain within 0.1 dBi of the theoretical values, the beam book is confirmed to be above the predetermined threshold.

Table 5.11: The gains of the calibrated beam book of 4-element array applying ON/OFF method having $0.5\lambda$ bent slab distortion and different irregular phase errors.

| - | $\text{Gain}_{theoretical}$ [dBi] | $\text{Gain}_{BS}$ [dBi] | $\text{Gain}_{irr1}$ [dBi] | $\text{Gain}_{irr2}$ [dBi] | $\text{Gain}_{irr3}$ [dBi] |
|---|---|---|---|---|---|
| $\theta = 54°$ | 21.94 | 21.95 | 21.96 | 21.96 | 21.95 |
| $\theta = 14°$ | 25.94 | 25.93 | 25.93 | 25.93 | 25.92 |
| $\theta = -22°$ | 25.31 | 25.31 | 25.29 | 25.28 | 25.31 |
| $\theta = -60°$ | 19.44 | 19.46 | 19.45 | 19.42 | 19.43 |

Table 5.12: The gains of the calibrated beam book of 8-element array applying ON/OFF method having $1.5\lambda$ bent slab distortion and different irregular phase errors

| - | $\text{Gain}_{theoretical}$ [dBi] | $\text{Gain}_{BS}$ [dBi] | $\text{Gain}_{irr1}$ [dBi] | $\text{Gain}_{irr2}$ [dBi] | $\text{Gain}_{irr3}$ [dBi] |
|---|---|---|---|---|---|
| $\theta = 56°$ | 27.70 | 27.71 | 27.72 | 27.71 | 27.73 |
| $\theta = 36°$ | 30.64 | 30.68 | 30.67 | 30.67 | 30.67 |
| $\theta = 18°$ | 31.93 | 31.95 | 31.92 | 31.92 | 31.95 |
| $\theta = 0°$ | 32.30 | 32.30 | 23.29 | 32.26 | 32.29 |
| $\theta = -18°$ | 31.72 | 31.74 | 31.73 | 31.76 | 31.75 |
| $\theta = -36°$ | 30.17 | 30.21 | 30.21 | 30.20 | 30.22 |
| $\theta = -58°$ | 26.17 | 26.23 | 26.24 | 26.20 | 26.24 |

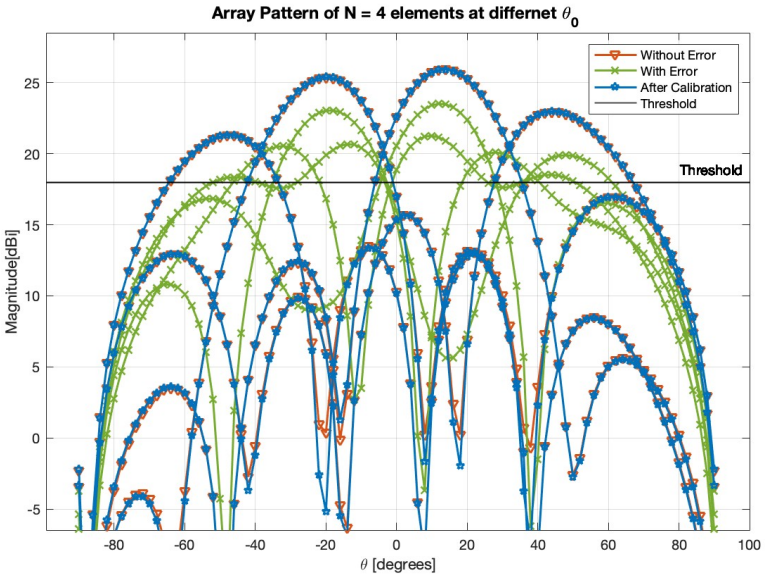


Figure 5.23: Beam book of the 4-element array showing degradation due to $0.5\lambda$ bent slab distortion in green, with the theoretical beam book in orange, and the calibrated beam book using the ON/OFF method depicted in blue, where all beams are calibrated above the predefined threshold of 18 dBi.

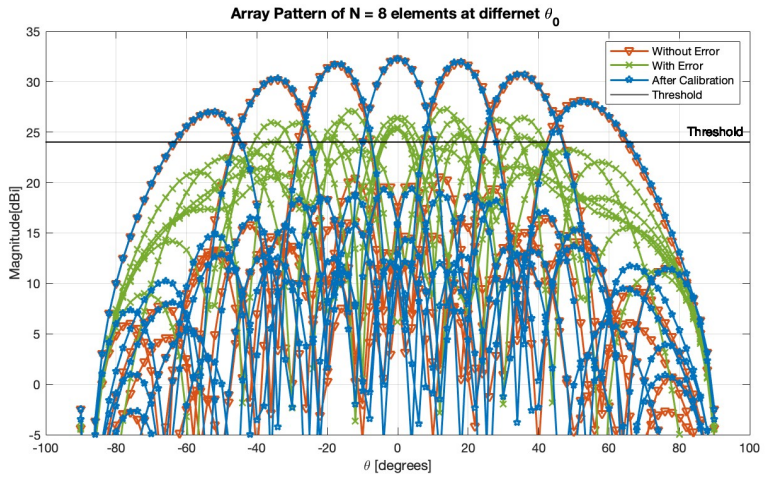


Figure 5.24: Beam book of the 8-element array showing degradation due to $1.5\lambda$ bent slab distortion in green, with the theoretical beam book in orange, and the calibrated beam book using the ON/OFF method depicted in blue, where all beams are calibrated above the predefined threshold of 24 dBi.

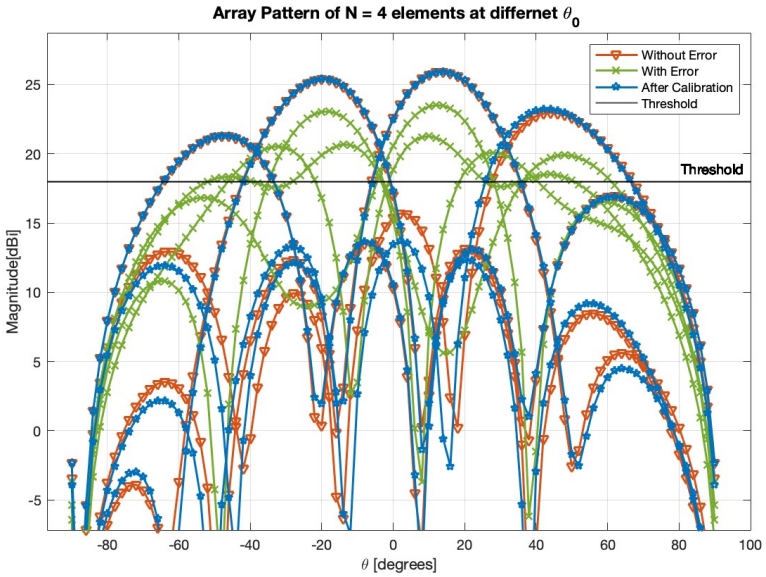


Figure 5.25: Beam book of the 4-element array showing degradation due to irregular phase error in green, with the theoretical beam book in orange, and the calibrated beam book using the ON/OFF method depicted in blue, where all beams are calibrated and above the predefined threshold of 18 dBi and the obtained gains noted as $\text{gain}_{irr3}$ in table 5.11.

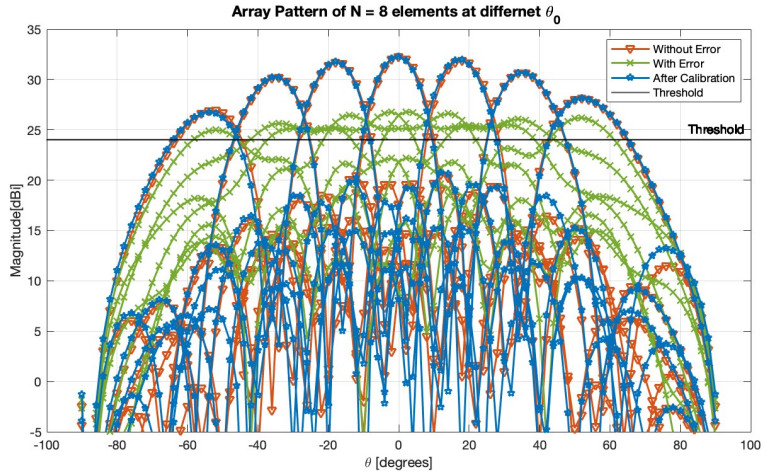


Figure 5.26: Beam book of the 8-element array showing degradation due to irregular phase error in green, with the theoretical beam book in orange, and the calibrated beam book using the ON/OFF method depicted in blue, where all beams are calibrated above the predefined threshold of 24 dBi and the obtained gains noted as $\text{gain}_{irr3}$ in table 5.12.

### 5.7.2 mREV Calibration Results

In this algorithm, all elements are activated, but calibration involves individually tuning each element's phase until maximum radiated power is achieved, which is

then recorded for that element. This procedure is repeated for each element until the entire array is calibrated. However, running the mREV algorithm just once reveals its inadequacy in calibration, as demonstrated by the gains deviating more than 0.1 dBi from the theoretical values due to deterministic errors like bent slab distortion and irregular phase errors, as shown in tables 5.13 and 5.14 for the 4- and 8-element arrays, respectively.

Table 5.13: The gains of the calibrated beam book of 4-element array applying mREV algorithm with one iteration, having $0.5\lambda$ bent slab distortion and different irregular phase errors. The values written in red indicate the cases where the gains deviate by more than 0.1 dBi from the theoretical values.

| - | $\text{Gain}_{theoretical}$ [dBi] | $\text{Gain}_{BS}$ [dBi] | $\text{Gain}_{irr1}$ [dBi] | $\text{Gain}_{irr2}$ [dBi] | $\text{Gain}_{irr3}$ [dBi] |
|---|---|---|---|---|---|
| $\theta = 54°$ | 21.94 | 21.95 | 21.84 | 21.63 | 21.80 |
| $\theta = 14°$ | 25.94 | 25.72 | 25.90 | 25.88 | 25.81 |
| $\theta = -22°$ | 25.31 | 25.14 | 25.09 | 25.29 | 25.16 |
| $\theta = -60°$ | 19.44 | 19.32 | 19.30 | 19.42 | 19.32 |

Table 5.14: The gains of the calibrated beam book of 8-element array applying mREV algorithm having $1.5\lambda$ bent slab distortion and different irregular phase errors. The values written in red indicate the cases where the gains deviate by more than 0.1 dBi from the theoretical values.

| - | $\text{Gain}_{theoretical}$ [dBi] | $\text{Gain}_{BS}$ [dBi] | $\text{Gain}_{irr1}$ [dBi] | $\text{Gain}_{irr2}$ [dBi] | $\text{Gain}_{irr3}$ [dBi] |
|---|---|---|---|---|---|
| $\theta = 56°$ | 27.70 | 27.61 | 27.63 | 25.59 | 27.61 |
| $\theta = 36°$ | 30.64 | 30.66 | 30.35 | 30.56 | 30.47 |
| $\theta = 18°$ | 31.93 | 31.93 | 31.78 | 31.85 | 31.88 |
| $\theta = 0°$ | 32.30 | 32.09 | 23.24 | 32.25 | 32.25 |
| $\theta = -18°$ | 31.72 | 31.69 | 31.74 | 31.69 | 31.72 |
| $\theta = -36°$ | 30.17 | 29.74 | 30.02 | 29.97 | 30.14 |
| $\theta = -58°$ | 26.17 | 26.20 | 26.14 | 26.17 | 26.18 |

Although the gains achieved after calibrating for bent slab distortion deviate by more than 0.1 dBi from theoretical values, the calibrated beam book shown in Figure 5.27 confirms that the gains throughout the coverage area consistently exceed the predetermined threshold. This is attributed to the tight beam configuration, which ensures that even the shifted beams post-calibration maintain gains above the threshold level. In this context, the shortcomings of mREV are more evident in the 8-element array when addressing the $1.5\lambda$ bent slab distortion, where the gains fall below the threshold at $\theta = -45°$, as illustrated in figure 5.28.

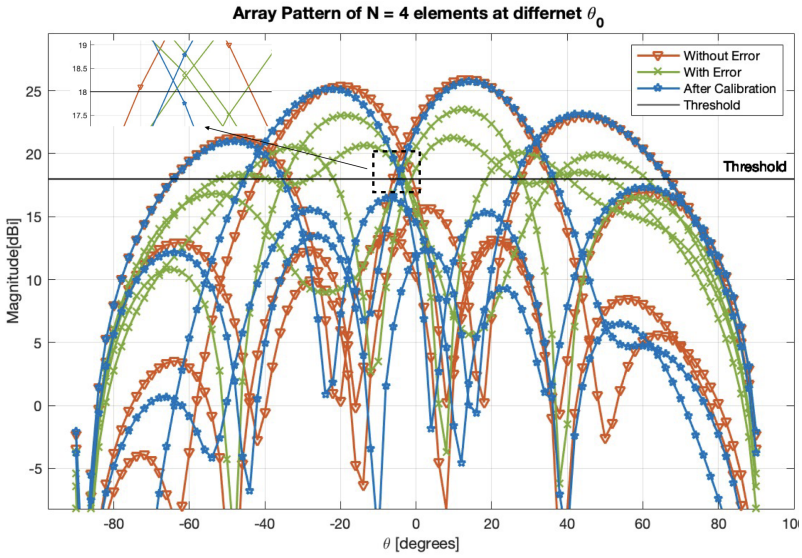


Figure 5.27: Beam book of the 4-element array showing degradation due to $0.5\lambda$ bent slab distortion in green, with the theoretical beam book in orange, and the calibrated beam book using the mREV method depicted in blue, where all beams are calibrated above the predefined threshold of 18 dBi.

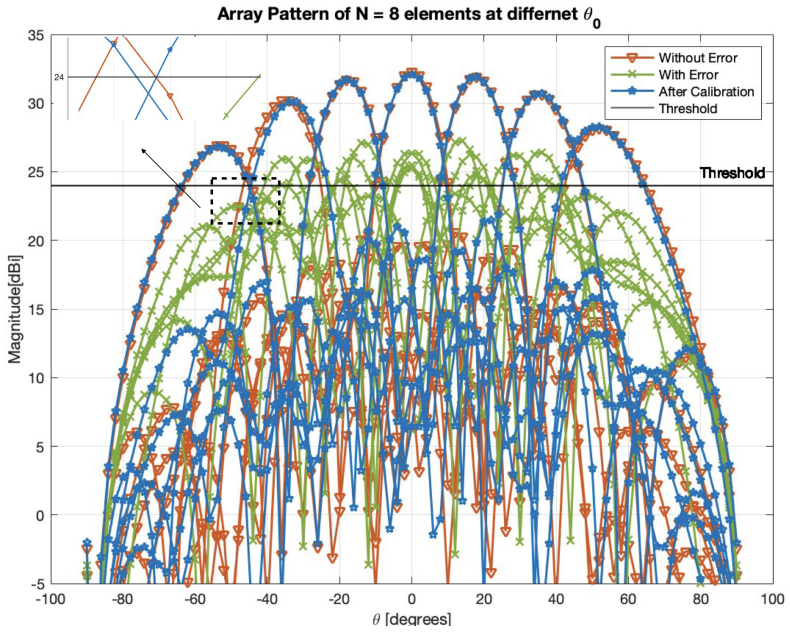


Figure 5.28: Beam book of the 8-element array showing degradation due to $1.5\lambda$ bent slab distortion in green, with the theoretical beam book in orange, and the calibrated beam book using the mREV method depicted in blue, where all beams are calibrated above the predefined threshold of 24 dBi.

An improvement for this algorithm is using the phase shifts determined in the initial calibration as starting values for subsequent runs. Tables 5.15 and 5.16 display the gains and the necessary number of runs to meet the criterion of not deviating more

than 0.1 dBi from the theoretical values. It becomes evident that mREV requires multiple runs for some beams to enhance performance and achieve gains that meet the criterion. When the 0.1 dBi gain difference condition is met, the resulting beam book surpasses the predefined threshold, as shown in figures 5.29 and 5.30 for the 4- and 8-element arrays, respectively, with bent slab distortion. A similar outcome is observed with irregular phase errors, as depicted in the beam books in figures 5.31 and 5.32 for the 4- and 8-element arrays, where the corresponding gains are noted in Tables 5.15 and 5.16 as $\text{gain}_{irr3}$.

Table 5.15: The gains of the calibrated beam book and the number of iterations, gain/iterations, of the 4-element array applying the iterative mREV algorithm having $0.5\lambda$ bent slab distortion and different irregular phase errors.

| - | $\text{Gain}_{theoretical}$ [dBi] | $\text{Gain}_{BS}$ [dBi] | $\text{Gain}_{irr1}$ | $\text{Gain}_{irr2}$ [dBi] | $\text{Gain}_{irr3}$ |
|---|---|---|---|---|---|
| $\theta = 54°$ | 21.94 | 21.95/1 | 21.89/2 | 21.92/1 | 21.93/2 |
| $\theta = 14°$ | 25.94 | 25.91/2 | 25.90/1 | 25.95/2 | 25.95/1 |
| $\theta = -22°$ | 25.31 | 25.31/2 | 25.22/2 | 25.28/1 | 25.23/1 |
| $\theta = -60°$ | 19.44 | 19.46/2 | 19.45/2 | 19.40/2 | 19.42/2 |

Table 5.16: The gains of the calibrated beam book and the number of iterations, gain/iterations, of the 8-element array applying the iterative mREV algorithm having $1.5\lambda$ bent slab distortion and different irregular phase errors.

| - | $\text{Gain}_{theoretical}$ [dBi] | $\text{Gain}_{BS}$ [dBi] | $\text{Gain}_{irr1}$ | $\text{Gain}_{irr2}$ [dBi] | $\text{Gain}_{irr3}$ |
|---|---|---|---|---|---|
| $\theta = 56°$ | 27.70 | 27.61/1 | 27.69/2 | 27.67/1 | 27.67/1 |
| $\theta = 36°$ | 30.64 | 30.66/1 | 30.65/1 | 30.63/1 | 30.65/1 |
| $\theta = 18°$ | 31.93 | 31.93/1 | 31.83/1 | 31.93/2 | 31.87/1 |
| $\theta = 0°$ | 32.30 | 32.31/2 | 32.22/1 | 32.28/1 | 32.29/2 |
| $\theta = -18°$ | 31.72 | 31.69/1 | 31.67/1 | 31.67/1 | 31.70/2 |
| $\theta = -36°$ | 30.17 | 30.14/2 | 30.07/1 | 30.18/1 | 30.13/1 |
| $\theta = -58°$ | 26.17 | 26.20/1 | 26.18/1 | 26.10/1 | 26.18/2 |

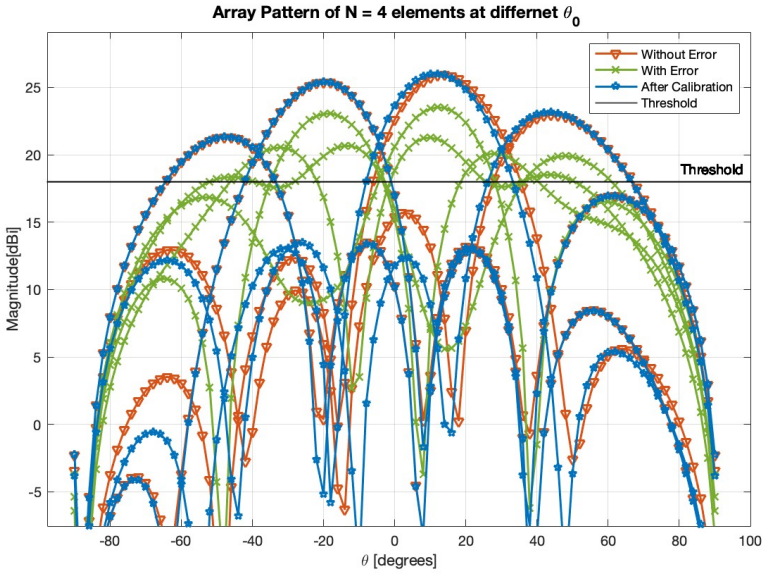


Figure 5.29: Beam book of the 4-element array showing degradation due to $0.5\lambda$ bent slab distortion in green, with the theoretical beam book in orange, and the calibrated beam book using the iterative mREV method depicted in blue, where all beams are calibrated above the predefined threshold of 18 dBi.

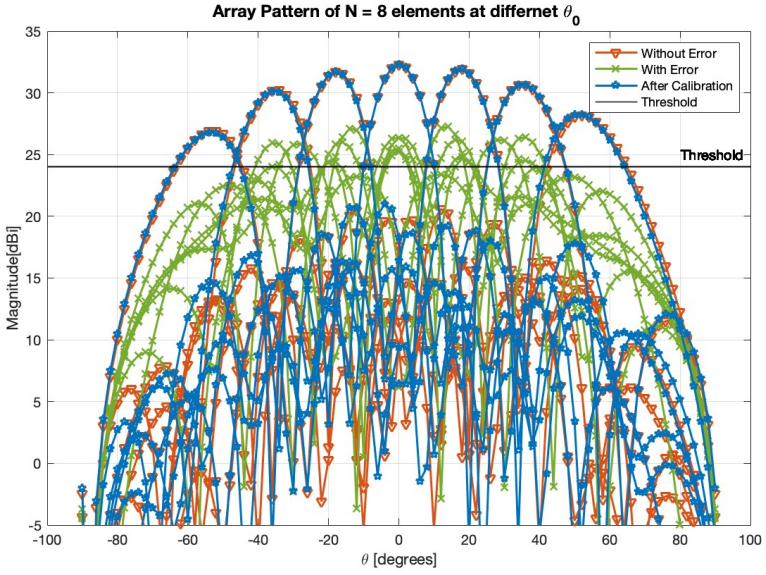


Figure 5.30: Beam book of the 8-element array showing degradation due to $1.5\lambda$ bent slab distortion in green, with the theoretical beam book in orange, and the calibrated beam book using the iterative mREV method depicted in blue, where all beams are calibrated above the predefined threshold of 24 dBi.

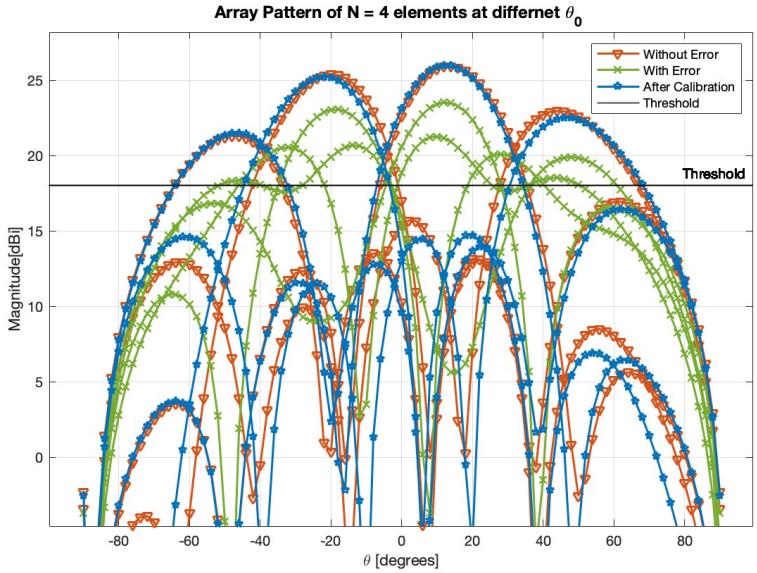


Figure 5.31: Beam book of the 4-element array showing degradation due to irregular phase error in green, with the theoretical beam book in orange, and the calibrated beam book using the iterative mREV method depicted in blue, where all beams are calibrated above the predefined threshold of 18 dBi and the obtained gains noted as $\text{gain}_{irr3}$ in table 5.15.

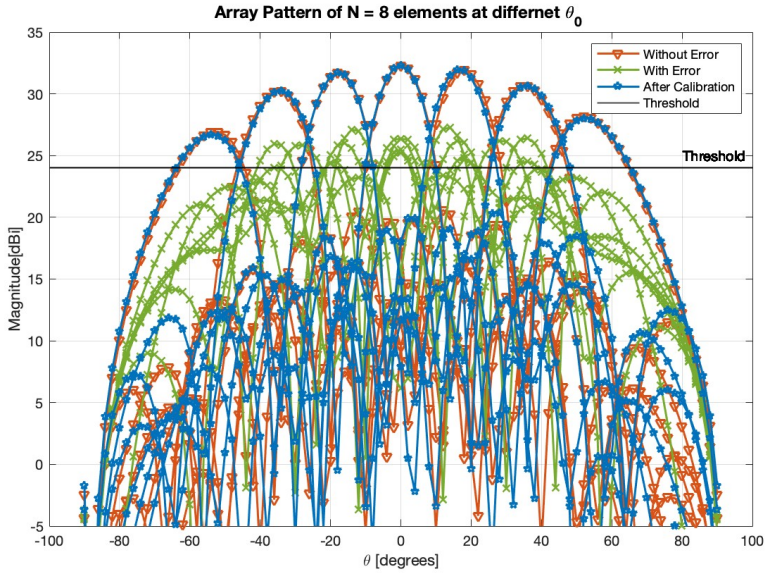


Figure 5.32: Beam book of the 8-element array showing degradation due to irregular phase error in green, with the theoretical beam book in orange, and the calibrated beam book using the iterative mREV method depicted in blue, where all beams are calibrated above the predefined threshold of 24 dBi and the obtained gains noted as $\text{gain}_{irr3}$ in table 5.16.

Observations indicate that utilizing more antenna elements results in a reduced

number of mREV iterations. To demonstrate this, mREV was executed 1000 times for calibrating the beam book of 4-, 8-, and 16-element arrays, each time experiencing different irregular phase errors within a range of ±6 radians. The findings, presented in Figure 5.33, illustrate a clear trend that increasing the number of array elements correlates with fewer mREV iterations. Specifically, only 20% of the beams in the 16-element array required two runs of the algorithm, compared to 34% for the 8-element array, and 48% for the 4-element array, which experienced the highest number of iterations. It is generally observed that no more than two iterations are needed, regardless of the array size.

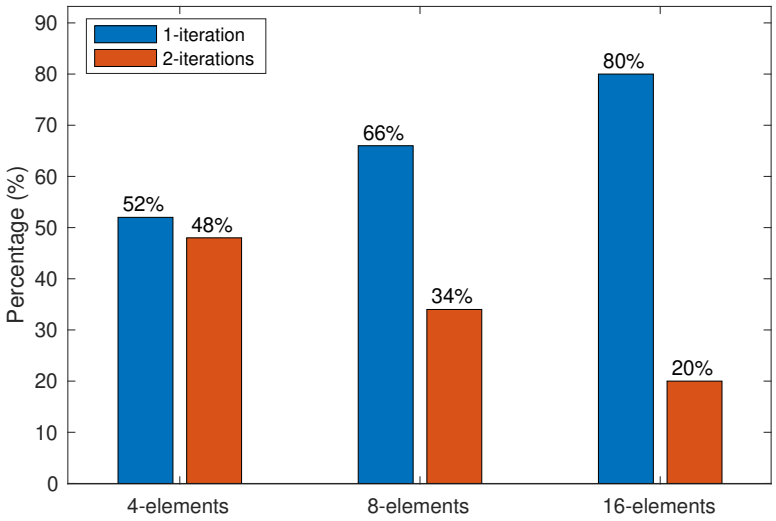


Figure 5.33: Bar chart showing the percentage of the number of iterations required to calibrate the beam books of 4-, 8- and 16-element arrays for 1000 different irregular phase errors

### 5.7.3 Enhanced Beam Book Calibration

The calibration of multiple beams is a time-consuming process. To mitigate this, an enhanced beam book is proposed, which includes more beams, but only a few are calibrated. The ON/OFF method, serving as the benchmark algorithm in this study, is used to calibrate the enhanced beam books for both 4- and 8-element arrays as detailed in section 4.3.1. Since systematic phase errors are difficult to determine analytically, various irregular phase errors were introduced to examine the calibration effectiveness.

With a set threshold of 18 dBi for the 4-element array, it is observed that full coverage within ±60° is achieved even with phase errors up to ±0.9 radians, tested across 1000 iterations. However, phase errors exceeding ±0.9 radians result in gains falling below the threshold at certain angles. Figure 5.34 shows a successful calibration of the enhanced beam book for the 4-element array. For the 8-element array, which has a gain threshold of 24 dBi, calibration ensures full coverage with irregular

phase errors of up to ±1 radians over 1000 iterations. One successful calibration demonstrating this is shown in Figure 5.35. Any errors exceeding this range result in gains that do not meet the threshold. This indicates that increasing the number of array elements from 4 to 8 elements reduces the sensitivity to phase errors. It should be noted that if the predefined threshold is set too high, lowering the threshold could allow for greater tolerance to higher phase errors.

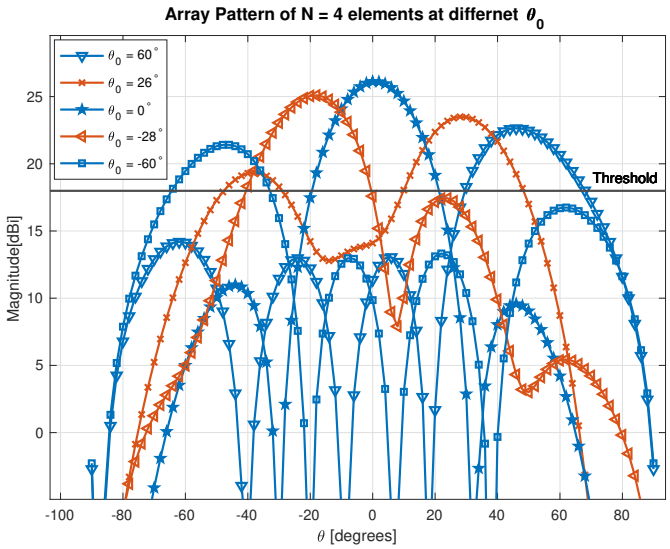


Figure 5.34: The calibrated enhanced beam book for a 4-element array, depicting irregular phase errors within the range of ±0.9 radians. Calibrated beams are shown in blue, while the uncalibrated beams are displayed in red.

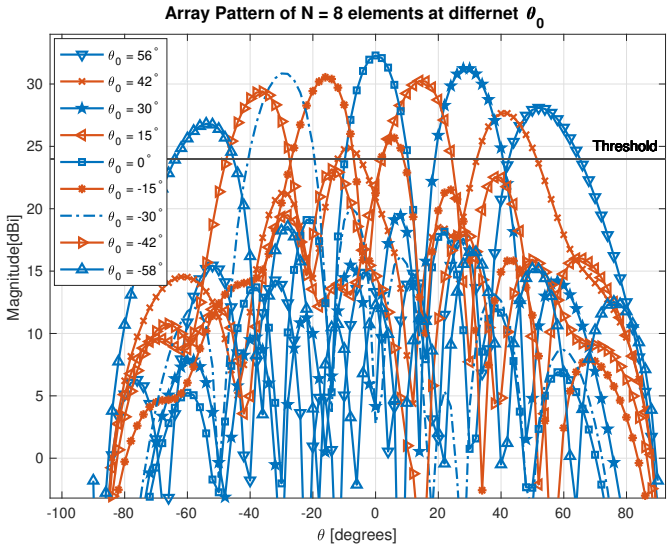


Figure 5.35: The calibrated enhanced beam book for a 8-element array, depicting irregular phase errors within the range of ±1 radians. Calibrated beams are shown in blue, while the uncalibrated beams are displayed in red.

# 6

# Conclusion

In conclusion, this thesis has successfully analyzed the construction and calibration of a 100 GHz transceiver providing a 10 GHz bandwidth. Focused on the optimal selection of components based on performance characteristics, the study also incorporated linear phased array antennas of varying sizes to thoroughly investigate the influence of different uncertainty sources on antenna performance. The research predominantly examined 4- and 8-element arrays, occasionally extending to 16-element arrays to gain deeper insights into the effects of array size on antenna behavior. A key aim was achieving a coverage range of $\pm 60^\circ$ through beamforming and beam steering in far-field scenarios using digital PS and attenuators. These digital components introduce quantization errors due to their limited bit resolution.

The results demonstrated that 4-bit phase shifters are sufficient to produce beam patterns for the 8-element array closely match theoretical predictions with only minimal deviations of 0.01 dBi and 0 dBi for the 4-element array. The study also revealed that amplitude perturbations of $\pm 1$ dB had a more pronounced impact on 8-element arrays, resulting in a greater degradation of gain and a maximum range loss of 5.1%. In contrast, 16-element arrays showed better tolerance to these perturbations, with a maximum range loss of 4%, though they were not as robust as 4-element arrays, which experienced a range loss of 2.39%.

The investigation into uncertainty sources identified impedance mismatches, temperature fluctuations, and structural manufacturing errors as significant factors. Impedance mismatches showed minimal loss impacts at the designed center frequency but were more pronounced at the bandwidth edges. Specifically, amplitude and phase deviations for the receiving chain at 95 GHz and 105 GHz were analyzed at $\pm 0.95/6.39^\circ$ and $\pm 0.77/5.16^\circ$, respectively, and for the transmitting chain, the deviations were $\pm 1.09/7.32^\circ$ and $\pm 0.63/4.16^\circ$. Assuming a tolerable range loss of less than 6%, these mismatches were deemed negligible across all studied arrays.

Temperature-related uncertainties required calibration for the 4-element array when phases varied by more than $\pm 0.5 \cdot 39^\circ$ at extreme temperatures of -45°C and 85°C. However, 8-element arrays showed reduced sensitivity to temperature-induced phase deviations, negating the need for calibration under similar conditions. Amplitude calibration was necessary when operating outside the -5°C to 65°C range where losses exceeded 6 %. Structural errors due to manufacturing required the development of two calibration algorithms, both effective in correcting phase errors regardless of size, with the mREV algorithm requiring multiple iterations for optimal pattern

alignment compared to the simpler ON/OFF method. It has been shown that using mREV, as the number of array elements increases, fewer iterations are required. After 1000 runs of different irregular phase errors in the range of ±6 radians, for a 4-element array, 48% of the beams required two iterations; for an 8-element array, 34% required two iterations; and for a 16-element array, only 20% of the beams required two iterations. Notably, no more than two iterations were needed to obtain the optimal pattern.

Finally, the thesis explored two types of beam books designed to achieve comprehensive coverage of ±60°. The first type required calibration of all beams, while the second, an enhanced beam book, applied calibration selectively to fewer beams, thereby reducing both time and effort involved in the calibration process. While the beam book of the 4-element array required the calibration of 5 beams, the enhanced beam book required calibration of only 3 beams. Similarly, the enhanced beam book of the 8-element array required the calibration of 5 beams, compared to 7 beams in the non-enhanced beam book. The analysis showed that for the enhanced beam book, the phase error tolerance for a 4-element array was limited to ±0.9 radians to maintain full coverage. Conversely, the 8-element array, which demonstrated lower sensitivity to phase errors, allowed for a greater phase error of up to ±1 radian.

This thesis underscores the critical relationship between array configuration, environmental influences, and calibration strategies in the development of high-frequency transceiver systems, providing significant contributions to the field and paving the way for future advancements in communication technology.

# 7

# Ethics

Although antenna calibration itself may not present direct ethical issues, it is a critical component of advanced communication systems, which encompass various ethical concerns that must be addressed. The development of such technologies, while making our lives easier, also contributes to the rise of cybercrimes. Additionally, many countries are advancing their cyber warfare capabilities, emphasizing the need for secure and resilient cyberspace and Information and Communication Technology (ICT) systems [60]. Ensuring that advanced communication systems are safe, secure, and accessible is of paramount importance. Data privacy is another significant ethical issue, necessitating robust data protection measures that safeguard individual privacy rights. Furthermore, the algorithms used in these communication systems must be free from bias to avoid discriminatory outcomes and ensure equitable treatment for all users. Addressing these ethical considerations is crucial in the responsible development and deployment of advanced communication technologies [61].

# 8

# Future Work

For future work, several areas require further investigation to refine the understanding and effectiveness of high-frequency transceiver systems. One critical aspect is the study of temperature drifts, particularly under conditions where temperature distribution is not uniform across the components. This involves assessing the impact of non-uniform temperature fields on calibration requirements and performance, as well as specifically examining the influence of temperature variations on amplifier behavior.

Additionally, the potential physical misalignment in the calibration chamber that impacts measurement accuracy needs thorough exploration. This will help in developing more robust calibration techniques that can compensate for setup irregularities and ensure the reliability of the measurements.

Gaining a deeper understanding of amplitude perturbation and its relationship to the number of array elements is necessary, particularly since 8-element arrays are most affected, while 4-element and 16-element arrays show less impact.

Moreover, since the current results were derived from Matlab simulations, it is imperative to extend this research to the calibration of real components. Practical testing of the calibration algorithms on actual hardware will validate the simulation outcomes and potentially reveal new challenges and solutions in the calibration process. This hands-on approach will significantly enhance the practical relevance and applicability of the research findings in real-world scenarios.

# Bibliography


[1] Bowen Zhu et al. "40-Gbit/s W-band Signal Delivery over 4600-m Wireless Distance Employing Advanced DSPs". In: *2022 IEEE International Conference on Communications Workshops (ICC Workshops)*. 2022, pp. 904–909. DOI: 10.1109/ICCWorkshops53468.2022.9814567.

[2] Tiago Varum, Amélia Ramos, and João N. Matos. "Planar microstrip series-fed array for 5G applications with beamforming capabilities". In: *2018 IEEE MTT-S International Microwave Workshop Series on 5G Hardware and System Technologies (IMWS-5G)*. 2018, pp. 1–3. DOI: 10.1109/IMWS-5G.2018.8484697.

[3] Nasser Ghassemi et al. "Low-Cost and High-Efficient W-Band Substrate Integrated Waveguide Antenna Array Made of Printed Circuit Board Process". In: *IEEE Transactions on Antennas and Propagation* 60.3 (2012), pp. 1648–1653. DOI: 10.1109/TAP.2011.2180346.

[4] Hanfeng Wang et al. "Photonics-Assisted Broadband Frequency-Hopping System for W-Band MMW Secure Communications". In: *2023 Asia Communications and Photonics Conference/2023 International Photonics and Optoelectronics Meetings (ACP/POEM)*. 2023, pp. 1–4. DOI: 10.1109/ACP/POEM59049.2023.10369691.

[5] Kuo-Ming Chen, Yun-Han Pan, and Ta-Sung Lee. "Low-Complexity Beam Selection for Hybrid Precoded Multi-User mmWave Communications". In: *2018 IEEE International Conference on Signal Processing, Communications and Computing (ICSPCC)*. 2018, pp. 1–5. DOI: 10.1109/ICSPCC.2018.8567785.

[6] Randy L. Haupt. "Array Beamforming Networks". In: *Antenna Arrays: A Computational Approach*. 2010, pp. 401–463. DOI: 10.1002/9780470937464.ch7.

[7] A. Slimani, S.D. Bennani, and A. El Alami. "Effect of inter-elements distance and phase shift excitation on radiation performance of linear, planar and circular arrays antennas ". In: *2017 International Conference on Wireless Technologies, Embedded and Intelligent Systems (WITS)*. 2017, pp. 1–7. DOI: 10.1109/WITS.2017.7934629.

[8] Chen Tengbo, Zhang Lu, and Du Hailong. "An Amplitude-phase Measurement Method of Phased Array Antenna Based on Self-Calibration RF Channel". In: *2018 10th International Conference on Communication Software and Networks (ICCSN)*. 2018, pp. 460–464. DOI: 10.1109/ICCSN.2018.8488296.

[9] Michelle Champion et al. “Array calibration and health/status check using a “reverse” transmit/receive module”. In: *2013 IEEE International Symposium on Phased Array Systems and Technology*. 2013, pp. 642–648. DOI: 10.1109/ARRAY.2013.6731905.

[10] Si Tang and Zhengpeng Wang. “Fast Phased Array Calibration Method Based on Multiple Measuring Probes”. In: *2020 IEEE 3rd International Conference on Electronic Information and Communication Technology (ICEICT)*. 2020, pp. 311–313. DOI: 10.1109/ICEICT51264.2020.9334371.

[11] Cheng-Nan Hu et al. “Coherent Phase Calibration of the 5G Massive MIMO Devices Using CATR OTA Test Method”. In: *2021 International Symposium on Antennas and Propagation (ISAP)*. 2021, pp. 1–2.

[12] Fengchun Zhang et al. “Improved Over-the-Air Phased Array Calibration Based on Measured Complex Array Signals”. In: *IEEE Antennas and Wireless Propagation Letters* 18.6 (2019), pp. 1174–1178. DOI: 10.1109/LAWP.2019.2911725.

[13] William Eisenstadt, Bob Stengel, and Bruce M. Thompson. *Microwave Differential Circuit Design Using Mixed Mode S-Parameters*. Artech House, 2006. ISBN: 9781580539340.

[14] Elya B. Joffe and Kai-Sang Lock. “Appendix F: Overview of S Parameters”. In: *Grounds for Grounding: A Circuit to System Handbook*. 2010, pp. 1045–1055.

[15] I. Long Stephen. “4.2 S-Parameters.” In: *Communication Electronics - RF Design with Practical Applications Using Pathwave/ADS Software*. River Publishers, 2023. ISBN: 978-1-5231-5645-0.

[16] Xianming Qing and Zhi Ning Chen. “Measurement Methods and Setups of Antennas at 60–325 GHz Bands”. In: *Substrate-Integrated Millimeter-Wave Antennas for Next-Generation Communication and Radar Systems*. 2021, pp. 25–54. DOI: 10.1002/9781119611165.ch2.

[17] Constantine A. Balanis. *Antenna Theory : Analysis and Design*. New York Academy of Sciences Series. John Wiley amp; Sons, Incorporated, 2016. ISBN: 9781119178989. URL: https://search.ebscohost.com/login.aspx?direct=true&db=cat07472a&AN=clec.EBC7104469&site=eds-live&scope=site&authtype=guest&custid=s3911979&groupid=main&profile=eds.

[18] “Design of Digital Phase Shifters for Multipurpose Communication Systems With MATLAB Design and Analysis Programs”. In: *Design of Digital Phase Shifters for Multipurpose Communication Systems With MATLAB Design and Analysis Programs*. 2022, pp. i–xxxii.

[19] Robert C. Hansen. *Phased Array Antennas*. Wiley telecom, 2010. ISBN: 9780470401026.

[20] Arik D. Brown. *Active Electronically Scanned Arrays: Fundamentals and Applications*. IEEE Press Wiley, 2022. ISBN: 9781119749059.

[21] Mu Fang et al. “1-Dimensional Wide Scanning Gap Waveguide Based Slot Array Antenna using Decoupling Technique for 100 GHz Applications”. In: *IEEE Transactions on Antennas and Propagation* (2024), pp. 1–1. DOI: 10.1109/TAP.2024.3372147.

[22] D. Müller et al. “A D-Band 180° phase shifter with very low amplitude- and phase-error”. In: *2014 9th European Microwave Integrated Circuit Conference*. 2014, pp. 174–177. DOI: 10.1109/EuMIC.2014.6997820.

[23] William E Hord. “Microwave and millimeter-wave ferrite phase shifters”. In: *Microw. J* 32 (1989), pp. 81–94.

[24] Clive Poole and Izzat Darwazeh. “Chapter 12 - Microwave transistors and MMICs”. In: *Microwave Active Circuit Analysis and Design*. Ed. by Clive Poole and Izzat Darwazeh. Oxford: Academic Press, 2016, pp. 395–437. ISBN: 978-0-12-407823-9. DOI: https://doi.org/10.1016/B978-0-12-407823-9.00012-3.

[25] Jie Zhou, Huizhen Jenny Qian, and Xun Luo. “A 9-Bit Vector-Sum Digital Phase Shifter Using High Resolution VGAs and Compensated Quadrature Signal Generator”. In: *2019 IEEE MTT-S International Microwave Conference on Hardware and Systems for 5G and Beyond (IMC-5G)*. 2019, pp. 1–3. DOI: 10.1109/IMC-5G47857.2019.9160356.

[26] Nathan Ida. “2.9.5 Attenuators.” In: *Open Resonator Microwave Sensor Systems for Industrial Gauging - A Practical Design Approach*. Institution of Engineering and Technology (The IET), 2018. ISBN: 978-1-5231-1677-5. URL: https://search.ebscohost.com/login.aspx?direct=true&db=edsknv&AN=edsknv.kt011LO1Y2&site=eds-live&scope=site&authtype=guest&custid=s3911979&groupid=main&profile=eds.

[27] *Micro and Nanoelectronics Devices, Circuits and Systems : Select Proceedings of MNDCS 2023*. Lecture Notes in Electrical Engineering. 1067. 2024. ISBN: 978-981-9944-95-8. URL: https://search.ebscohost.com/login.aspx?direct=true&db=edsbvb&AN=edsbvb.BV049358110&site=eds-live&scope=site&authtype=guest&custid=s3911979&groupid=main&profile=eds.

[28] Qingfeng Zhang et al. “Mechanism Analysis and Design of a Switched T-Type Attenuator With Capacitive Phase Compensation Technique”. In: *IEEE Microwave and Wireless Technology Letters* 33.10 (2023), pp. 1438–1441. DOI: 10.1109/LMWT.2023.3303181.

[29] Peng Gu, Dixian Zhao, and Xiaohu You. “A Wideband Low-Loss CMOS Attenuator With dB-Linear Gain Tuning for W-Band Applications”. In: *IEEE Transactions on Circuits and Systems II: Express Briefs* 70.9 (2023), pp. 3308–3312. DOI: 10.1109/TCSII.2023.3267147.

[30] Usama Bin Zaheer et al. “Design of Programmable Digital Control Attenuator for Microwave Receivers”. In: *2023 2nd International Conference on Emerging Trends in Electrical, Control, and Telecommunication Engineering (ETECTE)*. 2023, pp. 1–5.

[31] Jaco du Preez. *Millimeter-Wave Power Amplifiers. [electronic resource].* Signals and Communication Technology. Springer International Publishing, 2017. ISBN: 9783319621661. URL: https://search.ebscohost.com/login.aspx?direct=true&db=cat07472a&AN=clec.SPRINGERLINK9783319621661&site=eds-live&scope=site&authtype=guest&custid=s3911979&groupid=main&profile=eds.

[32] Teresa M. Braun and Walter R. Braun. "LOW-NOISE AMPLIFIER AND FREQUENCY CONVERTER". In: *Satellite Communications Payload and System*. 2021, pp. 146–174. DOI: 10.1002/9781119384342.ch6.

[33] Fabian Thome et al. "A W/F-Band Low-Noise Power Amplifier GaN MMIC with 3.5-5.5-dB Noise Figure and 22.8-24.3-dBm Pout". In: *2022 IEEE/MTT-S International Microwave Symposium - IMS 2022*. 2022, pp. 603–606.

[34] Joel Vuolevi and Timo Rahkonen. *Distortion in RF Power Amplifiers.* Artech House, 2003. ISBN: 9781580536295. URL: https://search.ebscohost.com/login.aspx?direct=true&db=cat07472a&AN=clec.EBC227661&site=eds-live&scope=site&authtype=guest&custid=s3911979&groupid=main&profile=eds.

[35] Howard Hausman. *Microwave Power Amplifier Design with MMIC Modules.* Artech House, 2018. ISBN: 9781630815257. URL: https://search.ebscohost.com/login.aspx?direct=true&db=cat07472a&AN=clec.EBC5528461&site=eds-live&scope=site&authtype=guest&custid=s3911979&groupid=main&profile=eds.

[36] Ibrahim Petricli, Domenico Riccardi, and Andrea Mazzanti. "D-Band SiGe BiCMOS Power Amplifier With 16.8dBm P1dB and 17.1 PAE Enhanced by Current-Clamping in Multiple Common-Base Stages". In: *IEEE Microwave and Wireless Components Letters* 31.3 (2021), pp. 288–291. DOI: 10.1109/LMWC.2021.3049458.

[37] Fengjuan Wang et al. "A Miniaturized Wideband SIR Interdigital Bandpass Filter With High Performance Based on TSV Technology for W-Band Application". In: *IEEE Transactions on Components, Packaging and Manufacturing Technology* 13.6 (2023), pp. 906–909. DOI: 10.1109/TCPMT.2023.3286829.

[38] Miguel A. Salas-Natera and Ramón Martínez Rodríguez-Osorio. "Analytical Evaluation of Uncertainty on Active Antenna Arrays". In: *IEEE Transactions on Aerospace and Electronic Systems* 48.3 (2012), pp. 1903–1913. DOI: 10.1109/TAES.2012.6237569.

[39] Hsi-Tseng Chou and Dun-Yuan Cheng. "Beam-Pattern Calibration in a Realistic System of Phased-Array Antennas via the Implementation of a Genetic Algorithm With a Measurement System". In: *IEEE Transactions on Antennas and Propagation* 65.2 (2017), pp. 593–601. DOI: 10.1109/TAP.2016.2635630.

[40] Miguel A. Salas-Natera et al. "Circularly Polarized Active Antenna Array System Calibration for Improved Axial Ratio Systems". In: *2019 13th European Conference on Antennas and Propagation (EuCAP)*. 2019, pp. 1–5.

[41] Nathan Ida. *Engineering Electromagnetics*. Springer, 2021. ISBN: 9783030155599. URL: https://search.ebscohost.com/login.aspx?direct=true&db=cat09075a&AN=clpc.oai.edge.chalmers.folio.ebsco.com.fs00001000.eb53f2c1.9df9.4424.a6f8.f0cc83767ee3&site=eds-live&scope=site&authtype=guest&custid=s3911979&groupid=main&profile=eds.

[42] H.S.C. Wang. "Performance of phased array antennas with mechanical errors". In: *IEEE Conference on Aerospace Applications*. 1990, pp. 317–318. DOI: 10.1109/AERO.1990.109094.

[43] Kaan Temir, Murat Sencer Akyüz, and Yaşar Kemal Alp. "Consideration of environmental and functional factors in calibration of antenna integrated active phased array transmitters". In: *2016 IEEE International Symposium on Phased Array Systems and Technology (PAST)*. 2016, pp. 1–5. DOI: 10.1109/ARRAY.2016.7832558.

[44] Virendra Kumar et al. "Thermal Equilibrium in T/R Module Operation and Active Phased Array Antenna Calibration". In: *2021 IEEE MTT-S International Microwave and RF Conference (IMARC)*. 2021, pp. 1–4. DOI: 10.1109/IMaRC49196.2021.9714589.

[45] Jun Su Park et al. "Evaluate the Cooling Performance of Transmit/Receive Module Cooling System in Active Electronically Scanned Array Radar". In: *Electronics* 10 (Apr. 2021), p. 1044. DOI: 10.3390/electronics10091044.

[46] Yan Wang et al. "Effect of Temperature on Electromagnetic Performance of Active Phased Array Antenna". In: *Electronics* 9 (July 2020), p. 1211. DOI: 10.3390/electronics9081211.

[47] Li Xu-ping et al. "Design and thermal-analysis of a slotted waveguide antenna array for W-band applications". In: *2012 International Conference on Microwave and Millimeter Wave Technology (ICMMT)*. Vol. 3. 2012, pp. 1–4. DOI: 10.1109/ICMMT.2012.6230193.

[48] Sihao Qian et al. "Investigation of the Performance of Antenna Array for Microwave Wireless Power Transmission Considering the Thermal Effect". In: *IEEE Antennas and Wireless Propagation Letters* 21.3 (2022), pp. 590–594. DOI: 10.1109/LAWP.2021.3139003.

[49] Chong Pan et al. "Phased Array Antenna Calibration Method Experimental Validation and Comparison". In: *Electronics* 12.3 (2023). ISSN: 2079-9292. URL: https://www.mdpi.com/2079-9292/12/3/489.

[50] Rui Long et al. "Multi-Element Phased Array Calibration Method by Solving Linear Equations". In: *IEEE Transactions on Antennas and Propagation* 65.6 (2017), pp. 2931–2939. DOI: 10.1109/TAP.2017.2694767.

[51] Seiji Mano and Takashi Katagi. "A method for measuring amplitude and phase of each radiating element of a phased array antenna". In: *Electronics and Communications in Japan (Part I: Communications)* 65.5 (1982), pp. 58–64. DOI: https://doi.org/10.1002/ecja.4410650508. eprint: https://onlinelibrary.wiley.com/doi/pdf/10.1002/ecja.4410650508. URL: https://onlinelibrary.wiley.com/doi/abs/10.1002/ecja.4410650508.

[52] J.J. Lee et al. "Near-field probe used as a diagnostic tool to locate defective elements in an array antenna". In: *IEEE Transactions on Antennas and Propagation* 36.6 (1988), pp. 884–889. DOI: 10.1109/8.1192.

[53] Xin Jin et al. "Fast and Accurate Near-Field Calibration Method for Phased Array Antennas". In: *2018 10th International Conference on Wireless Communications and Signal Processing (WCSP)*. 2018, pp. 1–5. DOI: 10.1109/WCSP.2018.8555608.

[54] Yusheng Zhang et al. "Phased Array Calibration Based on Measured Complex Signals in a Compact Multiprobe Setup". In: *IEEE Antennas and Wireless Propagation Letters* 21.4 (2022), pp. 833–837. DOI: 10.1109/LAWP.2022.3149966.

[55] Qihao Zhang et al. *An Antenna Array Initial Condition Calibration Method for Integrated Optical Phased Array*. Feb. 2019.

[56] M. Hossain et al. "A W-Band Transceiver Chip for Future 5G Communications in InP-DHBT Technology". In: *2020 15th European Microwave Integrated Circuits Conference (EuMIC)*. 2021, pp. 193–196.

[57] Yu-Xiao Tao et al. "Design and Fabrication of W band Heterogeneous Integrated Transceivers". In: *2020 IEEE MTT-S International Wireless Symposium (IWS)*. 2020, pp. 1–3.

[58] Xiaoxiong Gu et al. "A compact 4-chip package with 64 embedded dual-polarization antennas for W-band phased-array transceivers". In: *2014 IEEE 64th Electronic Components and Technology Conference (ECTC)*. 2014, pp. 1272–1277.

[59] Andreas Olk, Kais Ben Khadhra, and Thiemo Spielmann. "Highly accurate fully-polarimetric radar cross section facility for mono- and bistatic measurements at W-band frequencies". In: *2017 Antenna Measurement Techniques Association Symposium (AMTA)*. 2017, pp. 1–6. DOI: 10.23919/AMTAP.2017.8123697.

[60] *What are the challenges in developing 6G?* 2024. URL: https://telcomaglobal.com/p/what-are-the-challenges-in-developing-6g.

[61] *Ethical Considerations in the Development of 6G*. URL: https://www.telecomgurukul.com/post/ethical-considerations-in-the-development-of-6g.

DEPARTMENT OF ELECTRICAL ENGINEERING
CHALMERS UNIVERSITY OF TECHNOLOGY
Gothenburg, Sweden
www.chalmers.se


CHALMERS